Gens, A. *et al.* (2011). *Géotechnique* **61**, No. 5, 367–386 [**doi:** 10.1680/geot.SIP11.P.015]

Hydromechanical behaviour of a heterogeneous compacted soil: experimental observations and modelling

A. GENS*, B. VALLEJÁN*, M. SÁNCHEZ†, C. IMBERT‡, M. V. VILLAR§ and M. VAN GEET¶

The paper describes a theoretical and experimental study of the coupled hydromechanical behaviour of a compacted mixture of bentonite powder and bentonite pellets intended as sealing material in underground repositories for nuclear waste. One of the main advantages of the use of powder/pellets mixtures is the reduction of the compaction effort required to achieve the value of average dry density necessary to attain the required swelling potential. However, the heterogeneous fabric of the material requires special approaches in order to describe adequately its behaviour during hydration. A double porosity formulation is presented to account for the presence of two distinct structural levels in the material. Hydraulic equilibrium between the two porosities is not assumed; instead a water exchange term between them is postulated. The formulation is applied to the modelling of a number of one-dimensional swelling pressure tests performed in the CEA (Commisariat à l'Énergie Atomique, France) and CIEMAT (Spain) laboratories. A very satisfactory quantitative description of the experimental observations is obtained that includes a number of complex behaviour features such as size effects and non-monotonic development of swelling pressures. Some microfabric observations using X-ray tomography and mercury intrusion porosimetry lend support to the conceptual approach adopted. The formulation is then applied to the analysis of a long-term large-scale sealing test performed at the Hades underground facility in Belgium, using the same set of hydraulic and mechanical parameters employed in the modelling of the laboratory tests. Although the field observations exhibit a much higher degree of scatter, the basic behaviour of the field sealing test is satisfactorily simulated. A formulation that incorporates basic features of the microfabric of the mixture is thus able to span successfully over a large range of space and time scales.

KEYWORDS: compaction; expansive soils; fabric/structure of soils; full-scale tests; laboratory tests; partial saturation

La présente communication décrit une étude théorique et expérimentale du comportement hydromécanique mixte d'un mélange compacté de poudre et de granulés de bentonite utilisé comme matériau d'étanchéité dans des dépôts souterrains de déchets nucléaires. Un des principaux avantages de l'utilisation de mélanges poudre/granulés est la réduction du travail de compactage nécessaire pour réaliser la densité sèche moyenne requise pour obtenir le potentiel de gonflement spécifié. Toutefois, la structure hétérogène du matériau nécessite l'emploi de méthodes particulières pour la description adéquate de son comportement au cours de l'hydratation. On présente une formulation à double porosité pour prendre en considération la présence de deux niveaux structurels distincts dans le matériau. On ne suppose pas l'existence d'un équilibre hydraulique entre les deux porosités, mais on postule une condition d'échange d'eau entre elles. On applique la formulation pour la modélisation d'un certain nombre d'essais de pression de gonflement unidimensionnels effectués dans les laboratoires de la CEA (en France) et de CIEMAT (en Espagne). On obtient ainsi une description extrêmement satisfaisante des observations expérimentales , y compris un certain nombre de caractéristiques complexes du comportement, par exemple les effets de la taille et le développement non monotones des pressions de gonflement. Certaines observations des micro-tissus effectuées en tomographie aux rayons X et en porosimétrie par intrusion de mercure (MIP) soutiennent le principe conceptuel adopté. On applique ensuite la formulation à l'analyse d'un essai d'étanchéité à grande échelle et à long terme, effectuée dans l'installation souterraine Hades en Belgique, en utilisant le même ensemble de paramètres hydrauliques et mécaniques utilisé pour la modélisation des essais en laboratoire. Bien que les relevés sur le terrain présentent une diffusion bien plus élevée, on réalise une simulation satisfaisante du comportement de base de l'essai d'étanchéité sur le terrain. On dispose ainsi d'une formulation comprenant les caractéristiques de base du micro-tissu du mélange couvrant avec succès une vaste plage d'échelles spatiales et des temps.

INTRODUCTION

The construction of deep underground repositories for high-level nuclear waste requires the excavation of shafts, or ramps, as well as horizontal drifts that give access to the waste emplacement area. Much attention has been given to engineered barriers placed around the waste (Gens *et al.*, 1998; 2009b) but the sealing of access shafts and drifts to block potential preferential pathways for radionuclide migration is of comparable importance (IAEA, 1990; Gens, 2003). Compacted bentonite is often considered as a suitable backfill material, not only because of its low permeability and favourable retardation properties, but also for its capability, on hydration, to fill gaps and voids that may arise from excavation irregularities or other causes. Therefore, in order to ensure the long-term safety of the repository, the backfill material must have enough swelling potential upon hydration to perform the sealing function satisfactorily. As swelling potential depends essentially on the dry density of the sealing material (Imbert & Villar, 2006), it may be necessary

Manuscript received 3 March 2010; revised manuscript accepted 20 October 2010. Published online ahead of print 22 March 2011. Discussion on this paper closes on 1 October 2011, for further details see p. ii.

* Department of Geotechnical Engineering and Geosciences, Universitat Politècnica de Catalunya, Barcelona, Spain.
† Texas A & M University, College Station, USA.
‡ CEA (Commisariat à l'Énergie Atomique), Gif sur Yvette, France.
§ CIEMAT, Madrid, Spain.
¶ ONDRAF/NIRAS, Brussels, Belgium.

to apply a significant compaction effort in order to achieve an adequate density value. Often, this causes operational difficulties as it is difficult to ensure a uniform and intense compaction in enclosed, irregularly shaped spaces. Pre-compacted bentonite blocks are sometimes used but they leave gaps between them and they are also difficult to accommodate when shafts and drifts have uneven excavation surfaces, a feature that is almost unavoidable in many cases. An interesting alternative is to use, as sealing material, a mixture of bentonite powder and highly compacted bentonite pellets (Volckaert *et al.*, 1996). In this way, the average dry density is already quite high on placement due to the contribution of the high-density pellets. Consequently, only modest compaction efforts may be required after putting the material in place and, in any case, a minimum density is always ensured. As an example, Fig. 1 shows the sealing of an experimental shaft backfilled with a compacted mixture of bentonite powder and pellets.

The resulting material is obviously highly heterogeneous, consisting of a mixture of relatively low-density bentonite powder with high-density bentonite pellets. The behaviour of such material upon hydration is likely to be complex and must be properly understood if a sufficient degree of confidence in the design and performance of the seal is to be achieved. A conceptual framework leading to a good understanding of this behaviour should also be of benefit for other heterogeneous compacted materials, such as, for instance, the often-encountered case of compacted clayey soils containing large lumps of intact material.

In this paper, some basic features of the hydration behaviour of this heterogeneous compacted soil are presented first. Afterwards, the theoretical formulation required for the analysis of this type of material is briefly described. The formulation is then applied to the modelling of a series of one-dimensional swelling pressure tests performed in the laboratory. Finally, the analysis is upscaled to the description of a full-scale sealing test performed in an underground laboratory.

BASIC FEATURES OF THE BEHAVIOUR OF POWDER–PELLETS MIXTURES DURING HYDRATION

The behaviour of the powder–pellets mixture during hydration has been examined by means of laboratory swelling pressure tests (Imbert & Villar, 2006). Note that the hydration of a shaft or tunnel seal due to the inflow of host rock water is akin to a swelling pressure test due to the confinement provided by the excavation walls. Swelling pressure tests are, therefore, very appropriate to examine the behaviour relevant to seal hydration.

Mixtures of 50% bentonite powder and 50% bentonite pellets by dry weight have been tested. FoCa clay, a calcium bentonite from the Paris Basin, has been selected for the study. The major component of the clay fraction is an interstratified clay mineral of 50% calcium beidellite and 50% kaolinite. It has also a number of accessory minerals and the major exchangeable cation is Ca^{2+}. It also contains, in decreasing amounts, Mg^{2+}, Na^{+} and K^{+} (Volckaert *et al.*, 2000). Pellets are manufactured by dynamic compaction of the powder between two rotating wheels. The dimensions of the pellets (Fig. 2) are $25 \times 25 \times 15$ mm and their average dry density is $1{\cdot}89$ g/cm^3. Compaction water content lies in the range 4–5%.

The swelling pressure tests were performed in the laboratories of CEA (Commisariat à l'Énergie Atomique, France) and CIEMAT (Spain). Samples were statically compacted to the desired density and were subsequently tested in oedometers equipped with load cells. The specimens were hydrated from the bottom, sample deformation was prevented and the evolution of swelling pressure recorded. Water intake during the test was also measured. Because of the low permeability of the bentonite, tests had to be run over extended periods generally lasting several months. Deionised water was used for hydration as the water from the site where the in situ test has been performed has a very low salinity, thus minimising potential chemical effects on results. In fact, the influence of the salinity of the solution on swelling pressure has been considered negligible or small for highly compacted bentonites, especially when divalent cations predominate because diffuse double layers are poorly developed (Pusch, 1994; Castellanos *et al.*, 2008). The issue of chemical effects on the hydromechanical behaviour of bentonite has been discussed in detail in Guimarães *et al.* (2007).

Typical results of the oedometer swelling pressure tests are shown in Fig. 3. They correspond to specimens of different lengths (5, 10 and 12 cm) compacted to a common dry density of $1{\cdot}60$ g/cm^3. The diameter of the samples is 12 cm in order to accommodate a representative number of pellets. Several remarks can be made.

(*a*) The evolution of the swelling pressure is very characteristic suggesting a rather complex pattern of behaviour. Swelling pressure increases rapidly at the beginning of the test, until reaching a peak value. Afterwards, the measured pressure drops to a minimum

Fig. 1. Mixture of bentonite pellets and bentonite powder used as sealing material in an experimental shaft

Fig. 2. Pellets of FoCa clay used in the investigation. The dimensions of the pellets are 25 × 25 × 15 mm

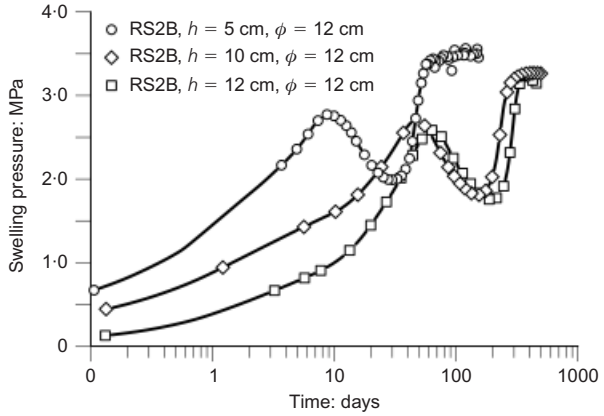

Fig. 3. Evolution of observed swelling pressures of a 50/50 powder/bentonite mixture. Tests performed at CEA laboratory at dry density of 1·60 g/cm^3

value to start later a new increase until reaching a stationary swelling pressure value at the end of the test. The same pattern of behaviour has been observed in the tests performed at other dry densities.

(*b*) There is a clear influence of the sample length on the rate of development of the swelling pressure. The longer the specimen, the slower the hydration kinetics is. This fact should be taken into account when transferring laboratory test results to field conditions where scale and hydration paths are bound to be quite different.

(*c*) The final swelling pressure at the end of the test is similar for the three samples, irrespective of length. Indeed, as Fig. 4 indicates, it has been found that final swelling pressure depends basically on dry density. It can be noted that the relationship between dry density and final swelling pressure for mixtures is very similar to that obtained in the same type of tests performed on samples of compacted bentonite powder (Imbert & Villar, 2006).

Interactions in the microfabric of the material during hydration must underlie the observed macroscopic behaviour. Direct observations of the hydration process were obtained by Van Geet *et al.* (2005) using microfocus X-ray computed tomography. A 50/50 powder–pellet mixture of FoCa clay at a dry density of 1·36 g/cm^3 and an average water content of 5·67% was placed in a methacrylate cylindrical cell. The sample was 7 cm high and 3·8 cm in diameter. Hydration was performed from the bottom of the sample under constant volume conditions. During the first 1·5 months, water was supplied at a very low pressure; afterwards water was injected at a pressure of 0·5 MPa during four additional months. A permeability determination was performed at the end of the test using a 0·6 MPa water pressure. X-ray tomography observations could be performed at specified time intervals. From the computation of the linear X-ray attenuation coefficient, the density distribution throughout the sample could be determined. Fig. 5 shows the density distribution on a vertical slice through the centre of the sample at different times of the experiment. It can be noted:

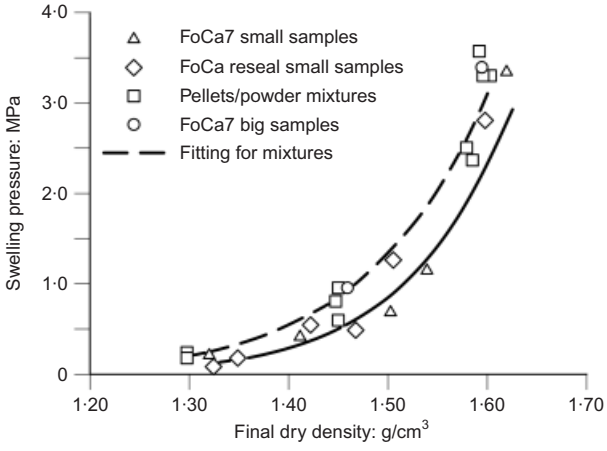

Fig. 4. Variation of swelling pressures of FoCa bentonite with dry density from tests performed in the CEA and CIEMAT laboratories. The dashed line corresponds to the relationship for 50/50 pellets/powder mixtures and the continuous line corresponds to compacted powder

(*a*) at the initial state there is a clear difference in density between pellets and powder

(*b*) during hydration, the density of the pellets reduces (swelling) whereas the density of the powder rises because of both soil compression and water content increase; the changes move gradually from bottom to top following the progress of hydration

(*c*) an apparently homogeneous specimen is obtained at the end of the test.

Further information is provided in Fig. 6 that shows the incremental density changes between the stages depicted in Fig. 5. It can be observed how hydration rises from the bottom of the specimen towards the top, causing density changes due to the swelling of the pellets and to the increase in saturation. Very little density change occurs after 2·5 months where the specimen has become much more homogeneous. It is also interesting to note that, in the initial stages of the test, the surfaces of the pellets away from the hydration front show some swelling due to the local exchange of water between powder and pellets.

THEORETICAL FORMULATION

Balance equations

The adoption of a double porosity model appears to be eminently suited to describe the heterogeneous nature of the material. Probably this concept was first introduced by Barrenblatt *et al.* (1960) (as quoted in Ghafouri & Lewis, 1996) to simulate flow through rigid, fissured porous media and it was later enlarged to consider the coupling between fluid flow and soil deformation (e.g. Aifantis, 1980; Wilson & Aifantis, 1982; Gens *et al.*, 1993; Khalili *et al.*, 1999; Callari & Federico, 2000). Here, the formulation developed in Sánchez (2004) is adopted.

The overall medium is assumed to consist of two overlapping but distinct continua. The macrostructure refers to the large-scale arrangement of soil particle aggregates and the relatively large pores between them. It is expected that, initially, most of the macrostructural pores belong to the bentonite powder. The microstructure refers to the clay particles and the micropores and interparticle spaces associated with them. A large proportion of the micropores lie initially in the high-density pellets but there will also be micropores in the clay particle aggregates present in the powder. Ideally, the microporosity of the powder aggregates should be distinguished from that in the pellets but, in that case, the number of interactions and parameters multiply leading to a cumbersome formulation that is difficult to apply in practice. As shown later, a double porosity model appears to be sufficient to describe the hydromechanical behaviour of the material. In the following, subscript M will stand for the macrostructure and subscript m for the microstructure. Accordingly, macroporosity and microporosity are

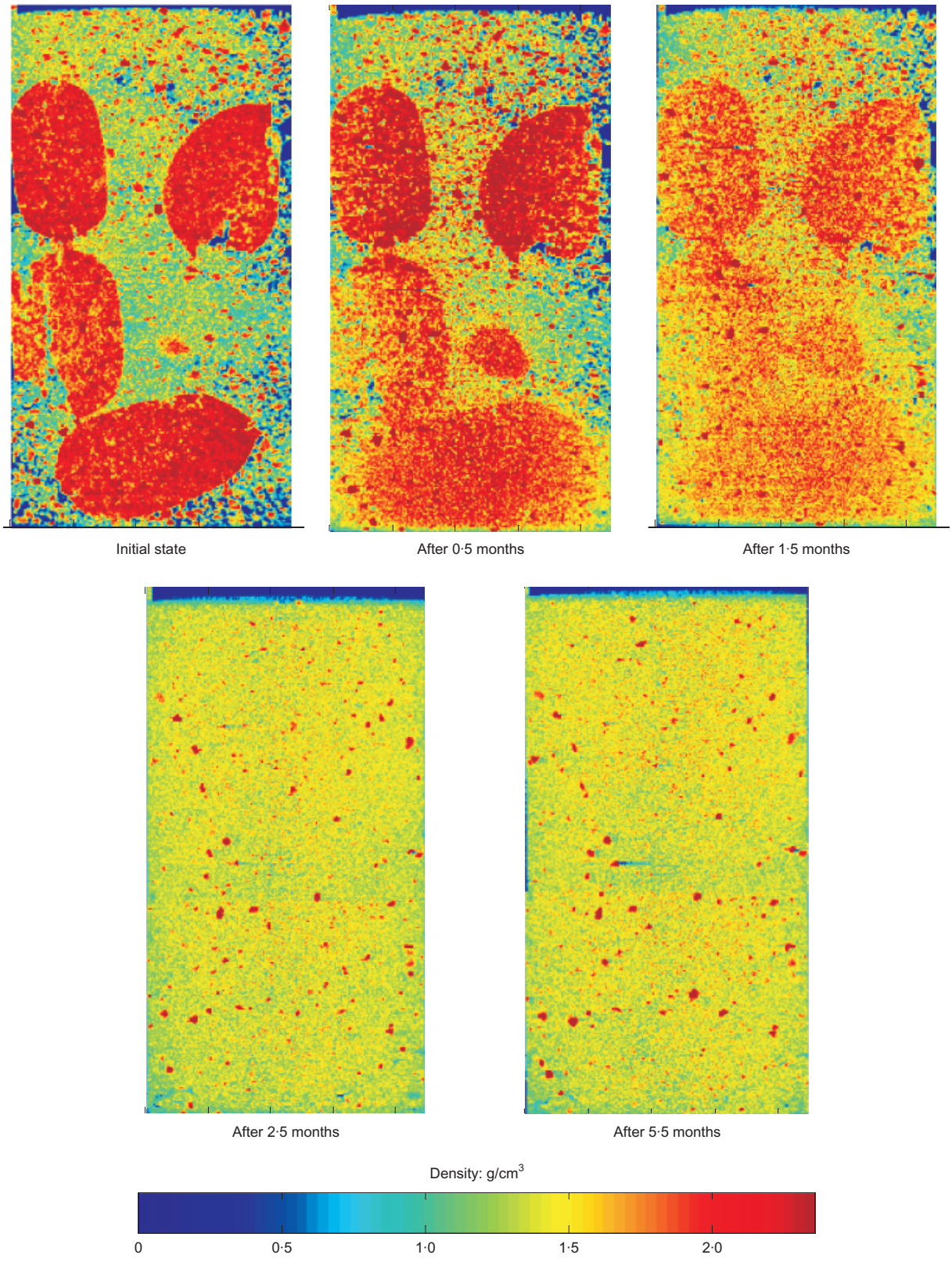

Fig. 5. Distribution of densities on a vertical slice through the centre of the sample observed at different stages of hydration (after Van Geet *et al.*, 2005). The specimen is 7 cm high and 3·8 cm in diameter

denoted as φ_M and φ_m respectively. Macroporosity and microporosity are defined as the volume of macropores and micropores, respectively, divided by the total volume of the soil. Thus, total porosity φ equals $\varphi_M + \varphi_m$. The degree of saturation of the macroporosity, S_{wM}, is the volume of macropores occupied by water over the volume of the macropores; an equivalent definition holds for the microporosity degree of saturation, S_{wm}.

An important feature is that hydraulic equilibrium between the two continua is not assumed; that is, at each point of the domain the water potentials in the two continua may be different, leading to an exchange of water between them (Fig.

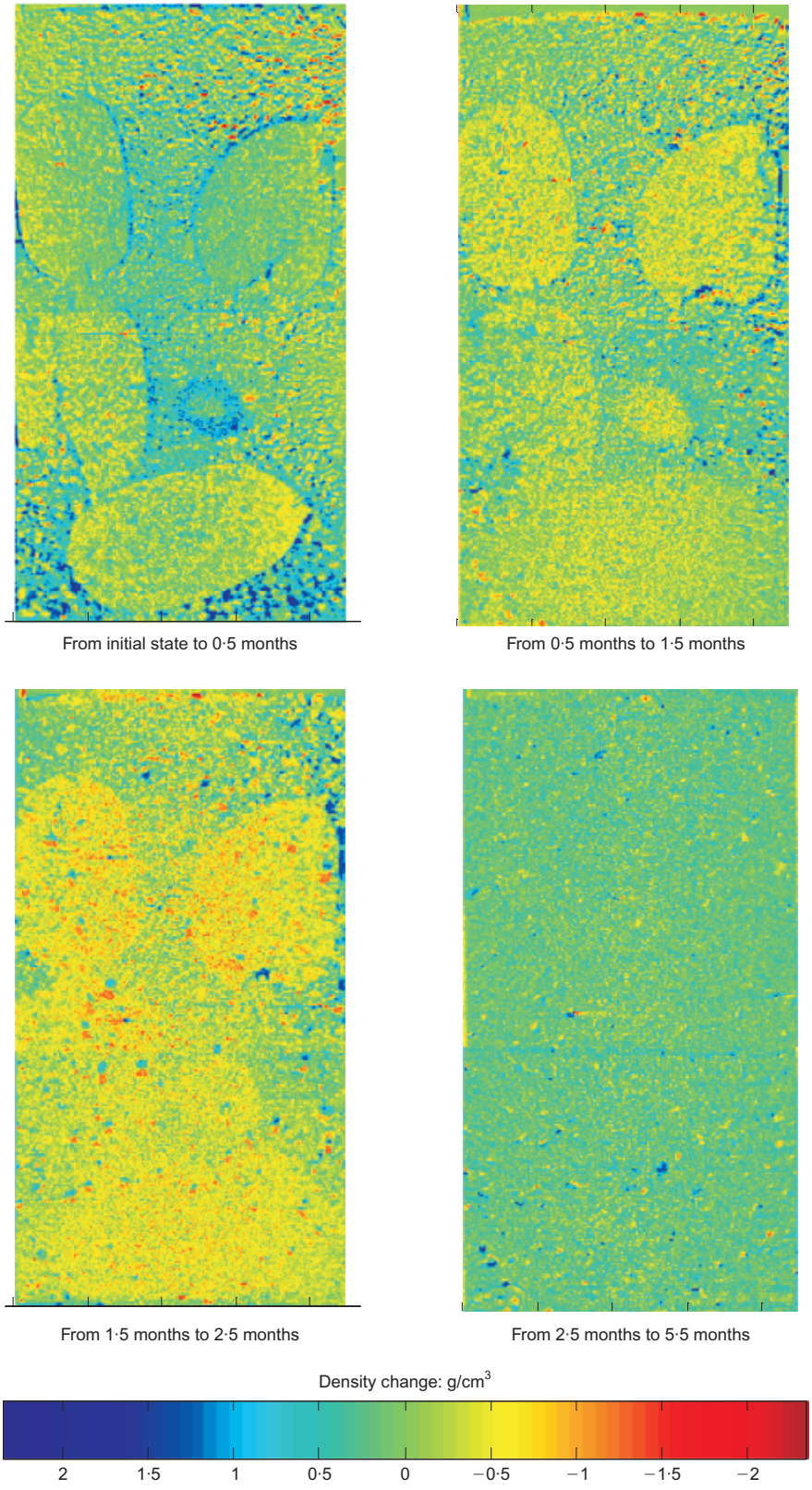

Fig. 6. Distribution of incremental density changes on a vertical slice through the centre of the sample observed at different stages of hydration (after Van Geet *et al.*, 2005). The specimen is 7 cm high and 3·8 cm in diameter

7). For simplicity, a linear relationship is assumed (e.g. Wilson & Aifantis, 1982) where water exchange is described by

$$\Gamma^{w} = \gamma(\psi_M - \psi_m) \tag{1}$$

where Γ^{w} is the water exchange term, γ is a parameter (often called the leakage parameter) and ψ is the total water potential. It is assumed that only matric and gravitational potential contribute to the total potential of the macrostructure but an additional osmotic component may also contribute to the microstructural potential (Gens, 2010). Here, potential is defined in pressure units. As the water exchange is local in space, the gravitational potential will be the same

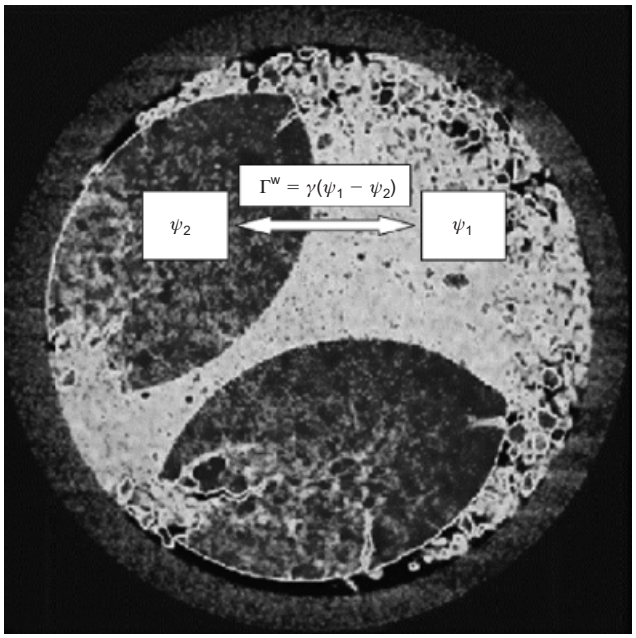

Fig. 7. Scheme of a double porosity material with a water exchange term

for the two media. Water exchange will therefore be driven by suction differences alone.

Using the concept of material derivative, the balance equation for the solid phase can be written, for the case of a single porosity medium, as:

$$\frac{\mathrm{D}\varphi}{\mathrm{D}t} = \frac{(1-\varphi)}{\rho_\mathrm{s}}\frac{\mathrm{D}\rho_\mathrm{s}}{\mathrm{D}t} + (1-\varphi)\,\dot{\varepsilon}_\mathrm{v} \tag{2}$$

where D(.)/Dt denotes material derivative, ρ_s is the solid density, $\dot{\varepsilon}_\mathrm{v}$ is the volumetric strain increment and t is time. For the case of double porosity equation (2) becomes (Sánchez, 2004)

$$\begin{aligned}\frac{\mathrm{D}\varphi}{\mathrm{D}t} = \frac{\mathrm{D}\varphi_M}{\mathrm{D}t} + \frac{\mathrm{D}\varphi_m}{\mathrm{D}t} = \frac{(1-\varphi)}{\rho_\mathrm{s}}\frac{\mathrm{D}\rho_\mathrm{s}}{\mathrm{D}t} \\ + (1-\varphi_M-\varphi_m)\,(\dot{\varepsilon}_{\mathrm{v}M} + \dot{\varepsilon}_{\mathrm{v}m})\end{aligned} \tag{3}$$

where it has been assumed that the total volumetric deformation is the sum of the volumetric deformations of each medium.

The water mass balance equation for the case of two overlapping flow media is

$$\frac{\partial}{\partial t}\left(\rho_\mathrm{w} S_{\mathrm{w}j}\phi_j\right) + \nabla\cdot\left(\boldsymbol{j}_{\mathrm{w}j}\right) \pm \Gamma^\mathrm{w} = f_j^\mathrm{w}; \qquad j = M,\, m \tag{4}$$

where $S_{\mathrm{w}j}$ is the liquid saturation of medium j, $\boldsymbol{j}_{\mathrm{w}j}$ is the total mass fluxes of water in the liquid phase and f_j^w is the external mass supply of water per unit volume in medium j. The possible presence of dissolved air in the liquid phase is neglected for simplicity.

Finally, it is assumed that total stresses for the overall medium affect equally the macro- and the microstructure. The equilibrium equation is

$$\nabla\cdot\boldsymbol{\sigma} + \boldsymbol{b} = \boldsymbol{0} \tag{5}$$

where $\boldsymbol{\sigma}$ is the total stress tensor and $\boldsymbol{b}$ is the vector of body forces. In contrast, the total deformation of the medium is obtained from the sum of the deformations of each domain.

To perform numerical analyses, this set of balance equations is incorporated into a computer code by way of a suitable discretisation procedure. The analyses reported in the paper have been performed with a modified version of Code_Bright (Olivella *et al.*, 1996) that incorporates the double porosity formulation.

Hydraulic constitutive equations

Liquid flow is governed by Darcy's law

$$\boldsymbol{q}_{\mathrm{w}j} = -\boldsymbol{K}_{\mathrm{w}j}\left(\nabla\psi_j\right) = -\boldsymbol{K}_{\mathrm{w}j}\left(\nabla p_{\mathrm{w}j} - \nabla\rho_{\mathrm{w}j}\boldsymbol{g}\right); \qquad j = M,\, m \tag{6}$$

where $\boldsymbol{q}$ is the mass liquid flow (with respect to the solid phase), $\boldsymbol{K}_\mathrm{l}$ is the liquid permeability tensor, p_l is the liquid pressure, ρ_l is the liquid density and $\boldsymbol{g}$ is the gravity vector. The permeability tensor is expressed as

$$\boldsymbol{K}_{\mathrm{w}j} = \boldsymbol{k}_j\frac{k_{\mathrm{r}j}}{\mu_j}; \qquad j = M,\, m \tag{7}$$

where $\boldsymbol{k}$ is the intrinsic permeability, k_r is the relative permeability that expresses the effect of degree of saturation (or suction) on global permeability and μ_j is the liquid viscosity. Intrinsic permeability depends on many factors such as pore size distribution, pore shape, tortuosity and porosity. Here a dependence of intrinsic permeability on porosity is adopted

$$\boldsymbol{k}_j = k_\mathrm{o}\exp\left(b(\phi_j - \phi_\mathrm{o})\right); \qquad j = M,\, m \tag{8}$$

where ϕ_o is a reference permeability for which the intrinsic permeability is k_o. Relative permeability is given by the empirical relationship

$$k_{\mathrm{r}j} = S_{\mathrm{e}j}^{\lambda}\,; \quad j = M,\, m \qquad S_\mathrm{e} = \frac{S_\mathrm{l} - S_\mathrm{lr}}{S_\mathrm{ls} - S_\mathrm{lr}} \tag{9}$$

where S_e is the effective degree of saturation, S_lr is the residual degree of saturation and S_ls is the degree of saturation in saturated conditions, normally taken as 1.

Finally the retention curve relates suction (or matric potential) with degree of saturation. There are a number of different expressions designed to fit experimentally determined retention curves. A modified form of the Van Genuchten (1980) law has been used here

$$S_{\mathrm{e}j} = \left[1 + \left(\frac{s}{P_\mathrm{o}}\right)^{1/(1-\lambda_\mathrm{o})}\right]^{-\lambda_\mathrm{o}}\left(1 - \frac{s}{P_\mathrm{d}}\right)^{\lambda_\mathrm{d}}; \qquad j = M,\, m \tag{10}$$

where s is the matric suction and P_o, P_d, λ_o and λ_d are model parameters.

Mechanical constitutive law

It has been postulated that the behaviour of highly expansive clays is better described assuming two levels of structure, a macrostructural level and a microstructural level, akin to the two porosities considered in the formulation just described (Gens & Alonso, 1992). In this work, the mathematical model formulated in terms of generalised plasticity (Sánchez *et al.*, 2005) is used.

The model assumes that the physicochemical phenomena occurring at the microstructural level are basically reversible and largely volumetric. Then the deformations arising from microstructural phenomena can be obtained from a non-linear elastic model dependent on a microstructural mean stress ($\hat{p}$) defined as

$$\hat{p} = p + s_m \tag{11}$$

where p is the net mean stress and s_m is the microstructural suction.

In the p–s plane, the line corresponding to constant microstructural mean stresses ($\hat{p}$) is referred to as the neutral loading line (F_{NL}) since no microstructural deformation occurs when the stress path moves on it (Fig. 8(a)). The neutral loading line (NL) divides the p–s plane into two parts, defining two main microstructural stress paths: a microstructural contraction path (MC, $\dot{\hat{p}} > 0$) and a microstructural swelling path (MS, $\dot{\hat{p}} < 0$).

The increment of the microstructural elastic deformation is expressed as a function of the increment of the microstructural mean stress

$$\dot{\varepsilon}_{vm} = \frac{\dot{\hat{p}}}{K_m}; \quad K_m = \frac{1 + e_m}{\kappa_m}\hat{p} \tag{12}$$

where $\dot{\varepsilon}_{vm}$ is the microstructural volumetric strain increment, K_m is the microstructural bulk modulus, e_m is the microstructural void ratio and κ_m is a model parameter. The behaviour of the macrostructural level is defined by the Barcelona basic model (BBM) (Alonso *et al.*, 1990). For completeness, the main BBM equations are presented in the Appendix.

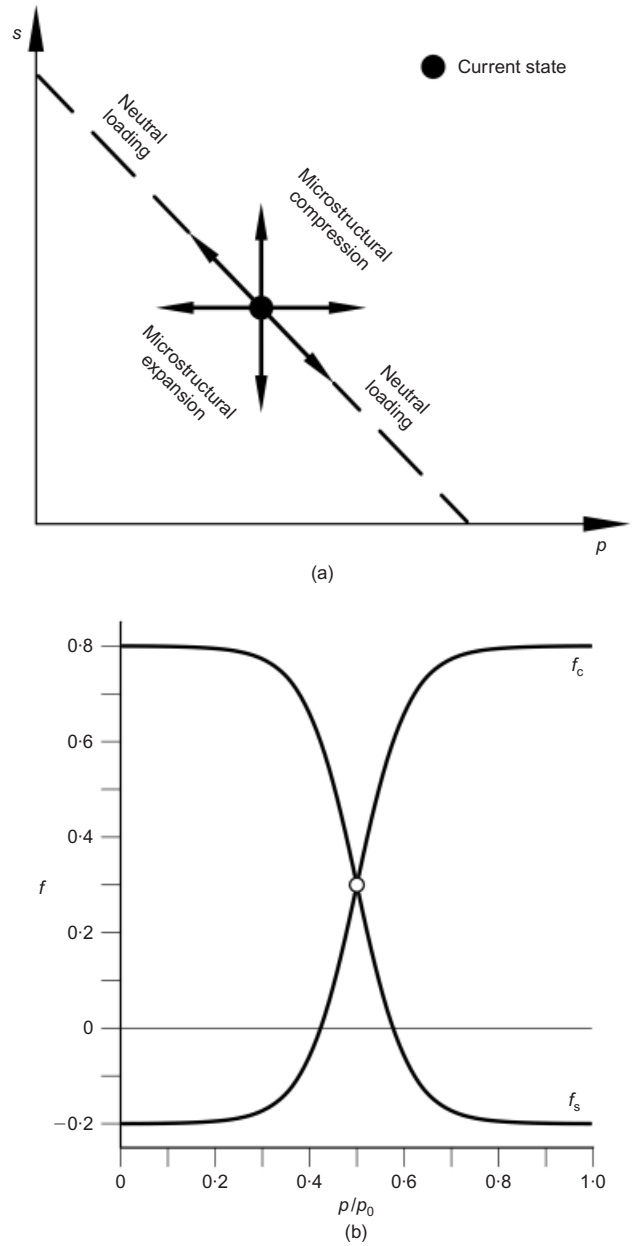

Fig. 8. Double structure mechanical constitutive law for expansive clays: (a) microstructural model; (b) interaction functions

A fundamental assumption of the framework is that microstructural behaviour is not affected by the macrostructure state but it only responds to changes in the driving variables (i.e. stresses and suction) at local microstructural level. In contrast, plastic macrostructural strains may result from deformations of the microstructure. It is postulated that plastic macrostructural strains can be expressed as

$$\dot{\varepsilon}^{p}_{vM} = f\dot{\varepsilon}_{vm} \tag{13}$$

where $\dot{\varepsilon}^{p}_{vM}$ is the macrostructural plastic strain arising from the deformation of the microstructure. Two interaction functions f are defined: f_c for MC paths and f_s for MS paths (Fig. 8(b)). In the case of isotropic loading, the interaction functions depend on the ratio p/p_o where p_o is the yield mean net stress at the current macrostructural suction value. The ratio p/p_o is a measure of the degree of openness of the macrostructure relative to the applied stress state. When this ratio is low it implies a dense packing of the material, it is then expected that the microstructural swelling (MS path) will affect strongly the global arrangements of clay aggregates, inducing large macrostructural plastic strains. If the p/p_o ratio comes close to 1, the state of the material approaches the BBM loading–collapse (LC) yield surface and it becomes collapsible. In that case, the multiplying effect of microstructural strains may be small or even negative. In this work, the following form of interaction function has been used

$$f_\alpha = f_{\alpha 0} + f_{\alpha i}\left(1 - \frac{p}{p_o}\right)^{n_\alpha}; \quad \alpha = s \text{ (swelling)}, \ c \text{ (contraction)} \tag{14}$$

Although this form of formulating the interplay between microstructure and macrostructure is conceptually quite simple, it has proved able to accommodate a wide range of different interaction phenomena (Gens & Alonso, 1992).

MODELLING SWELLING PRESSURE TESTS

Features of the tests and model parameters

The formulation outlined above has been applied to the modelling of a number of swelling pressure tests performed on specimens of 50/50 powder/pellets mixtures compacted to two different densities (1·45 g/cm^3 and 1·60 g/cm^3) and with a range of different lengths. The main characteristics of the tests are given in Table 1. The pellets always have the same density; the variation in the density of the samples arises from the different initial powder densities.

According to the formulation, it is necessary to estimate the initial microstructural and macrostructural porosity both in the pellets and in the powder. Mercury intrusion porosimetries (MIPs) were performed on the pellets, a typical result is shown in Fig. 9. There is always some degree of arbitrariness in the distinction between the two types of pores, pore size distribution being a continuum. Here, a pore size of 100 nm has been selected for this purpose based on the fact that there is a clear change of slope in the pore size density functions determined experimentally. This value is also consistent with other previous estimations in similar materials (Touret *et al.*, 1990; Romero, 1999; Lloret *et al.*, 2003). For the powder, the distinction between porosities was made on the bases of experimental pore size determinations reported previously (Romero, 1999; Marcial, 2003)

Table 1. Main characteristics of the swelling pressure tests

Test label	Sample height: mm	Diameter: mm	Void ratio of sample	Dry density of sample: g/cm^3	Initial water content of sample: %	Dry density of pellets: g/cm^3	Initial water content of pellets: %	Dry density of powder: g/cm^3	Initial water content of powder: %	Laboratory
MGR7	50	100	0·84	1·45	8·30	1·89	4·60	1·175	12·00	CIEMAT
MGR9	100	100	0·84	1·45	5·25	1·89	5·00	1·182	5·80	CIEMAT
RS2J	50	120	0·84	1·45	4·78	1·89	4·00	1·175	5·00	CEA
RS2B	50	120	0·67	1·60	8·07	1·89	4·31	1·385	11·83	CEA
RS2E	100	120	0·67	1·60	4·78	1·89	4·49	1·390	5·07	CEA
RS2F	120	120	0·67	1·60	4·78	1·89	4·49	1·390	5·07	CEA

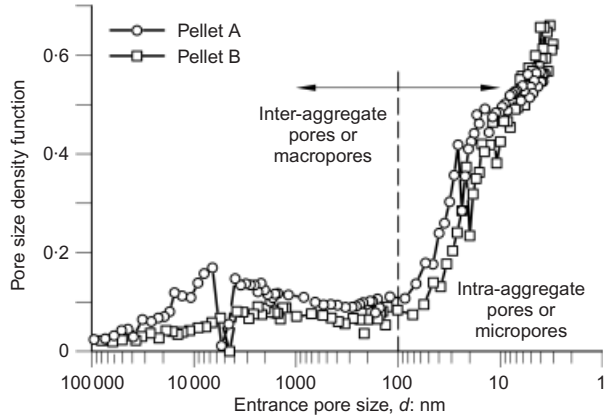

Fig. 9. Pore size density functions for two pellets

using the same threshold value. From this ensemble of results, it was found that the proportion of microporosity with respect to total porosity of compacted samples could be closely approximated by

$$v_m/v_T = 0{\cdot}0632\,\gamma_d^{3{\cdot}89} \tag{15}$$

where γ_d is the dry density in g/cm^3, v_m is the microstructural pore volume and v_T is the total pore volume. Fig. 10 shows the assumed variation of the different porosities (and void ratios) with as-compacted dry density. It is apparent that microporosity increases significantly in the highly compacted samples both in absolute and relative terms. Lacking more specific information, the initial proportions of water in the microstructure and in the macrostructure are assumed to be similar to those of the porosity components.

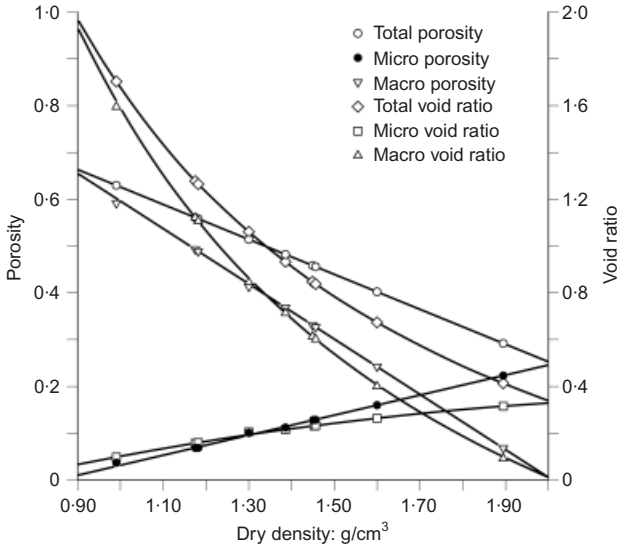

Fig. 10. Relationship between micro, macro and total porosities and dry density after compaction

The hydraulic parameters are presented in Table 2. There have been quite a number of determinations of the retention curve of compacted FoCa clay at different densities. They are shown in Fig. 11 together with the retention curves adopted in this work. The retention curves' parameters for the micro- and macroporosity have been estimated from the results of the higher and the lower density samples, respectively, as micropores are dominant in the high-density specimens and macropores predominate in the low-density specimens. Intrinsic permeability values and their variation have been derived from laboratory permeability tests on compacted FoCa clay at different dry densities, the results of which are summarised in Gens *et al.* (2009a). For relative permeability, an exponent value of 3 is adopted for the macrostructure, a value that has been obtained in several infiltration tests on homogeneous compacted bentonite (Gens *et al.*, 2009a). A lower exponent is assumed for the microstructure as it is conjectured that unsaturation has a lower impact on water mobility in the vicinity of clay particle surfaces. The leakage parameter is sometimes associated with some geometric characteristics of the medium, such as the specific surface of the matrix block (Barrenblatt *et al.*, 1960), the number of fractures and fracture intervals (Warren & Root, 1963) or the average size of clay blocks (Callari & Federico, 2000). Because of lack of relevant geometric information in this case, the leakage parameter was obtained from back-analysis and the same value was used in all the analyses. It should be recalled that, although most of the microporosity is initially present in the pellets, there is also some microporosity in the powder. Therefore, water exchanges between porosity levels will take place both in the powder and the pellets with, probably, some differences in the kinetics. However, a single leakage parameter has been used in the analyses for simplicity.

The parameters of the mechanical constitutive model are collected in Table 3. They were determined from back-calculation of laboratory oedometer tests on compacted FoCa clay (Volckaert *et al.*, 2000; Yahia-Aïssa *et al.*, 2000; Cui *et al.*, 2002). It should be noted that only one interaction function is required as only the microstructural swelling mechanism is engaged in the swelling pressure test. It should be stressed that although some BBM parameters of the macrostructure depend on the initial density of the powder, the parameters characterising the behaviour of the microstructure remain unchanged throughout all the analyses performed.

Swelling pressure tests at dry density 1·45 g/cm^3

Tests MGR7, RS2J and MGR 9 were performed on samples with a dry density of 1·45 g/cm^3. The estimated initial porosities and suctions are listed in Table 4. Figs

Table 2. Hydraulic parameters

Constitutive law	Expression	Parameter	Micro	Macro
Retention curve	$S_e = \frac{S_l - S_{lr}}{S_{ls} - S_{lr}} = \left[1 + \left(\frac{s}{P_o}\right)^{1/(1-\lambda_o)}\right]^{-\lambda_o} \left(1 - \frac{s}{P_d}\right)^{\lambda_d}$	P_o: MPa λ_o P_d: MPa λ_d S_{ls} S_{lr}	378·95 0·899 800 2·243 1·0 0·0	15 0·064 750 3·899 1·0 0·0
Intrinsic permeability High-density samples, $\gamma_d > 1{\cdot}60$ g/cm^3 $\boldsymbol{k}_j = k_o \exp(b(\phi_j - \phi_o))$		k_o: m^2 ϕ_o b	$2{\cdot}9 \times 10^{-20}$ 0·40 8·00	
Low-density samples, $\gamma_d < 1{\cdot}60$ g/cm^3 $\boldsymbol{k}_j = k_o \exp(b(\boldsymbol{\phi}_j - \boldsymbol{\phi}_o))$		k_o: m^2 ϕ_o b	$2{\cdot}9 \times 10^{-20}$ 0·40 11·00	
Relative permeability $k_r = S_e^{\lambda}$		λ S_{ls} S_{lr}	1·15 1·00 0·00	3·00 1·00 0·00
Leakage parameter $\Gamma^w = \gamma(\psi_1 - \psi_2)$		γ: kg s^{-1} m^{-3} MPa^{-1}	$5{\cdot}00 \times 10^{-5}$	

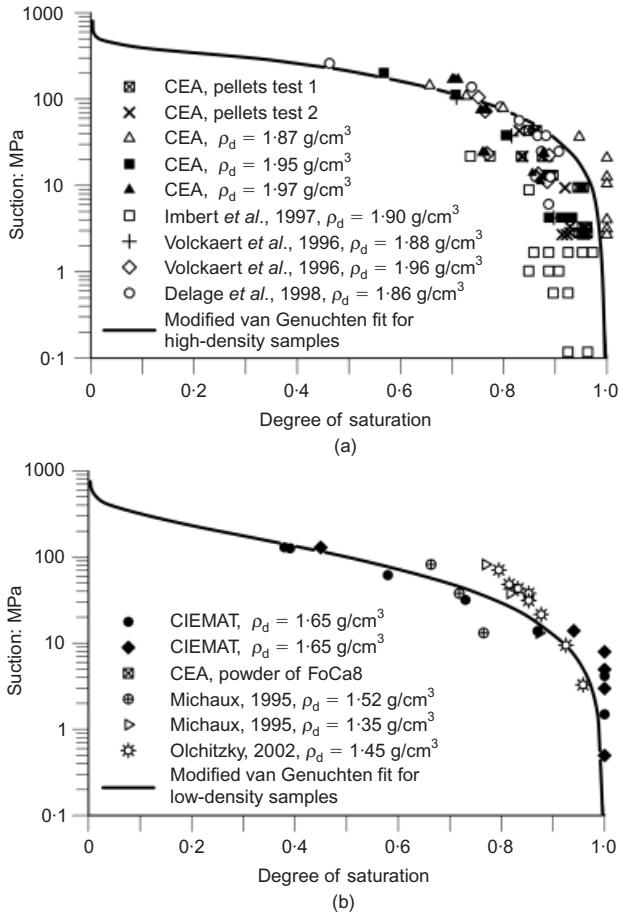

Fig. 11. Retention curves for FoCa clay: (a) samples with dry densities in the range 1·65–2·0 g/cm^3; (b) samples with dry densities in the range 1·35–1·65 g/cm^3

12(a)–12(c) show the computed evolution of swelling pressures compared with the measured values. Tests were run until macroscopic observations indicated that stationary conditions were achieved; test durations were over 200 days for the 5 cm long samples and 570 days for the 10 cm long sample.

In general, the rate of swelling pressure development at the start of the tests is underestimated by the analyses but the magnitude of the first peak and the time required to reach it are adequately reproduced by the calculations. Subsequent behaviour is also well modelled, including the observed reduction of swelling pressure and the final rise to the final steady-state value. In spite of having two different lengths, the pattern of behaviour is very similar in all three tests although, of course, the times required to reach the first peak and the stationary condition are longer for the taller specimen (MGR9). The swelling pressure rise in test MGR7 at day 120 is due to an increase of the injected water pressure. This pressure increase stage was not applied in the other tests. Figs 12(d)–12(f) indicate that the water intake of the tests is also well reproduced although, again, it can be noted that the observed rate of water inflow is larger than the computed value at the initial stages of the tests.

As the modelling appears to represent satisfactorily the real system, interesting information might be obtained by analysing in more detail some of the results of the analyses. For space reasons, attention is focused on test MGR9, but results from other tests are used when required. Fig. 13(a) shows the time evolution of macrostructural and microstructural suctions at three different points of sample MGR9: near the bottom hydration boundary (vertical coordinate $y = 0{\cdot}0$ m), at the centre of the sample ($y = 0{\cdot}05$ m) and near the top of the sample ($y = 0{\cdot}0975$ m). It can be observed that, at the bottom boundary, the macrostructural and microstructural suctions reduce rapidly, but they differ at the beginning of the test because of the delay in water transfer

Table 3. Parameters of the mechanical constitutive model

Constitutive law	Expression	Parameter	Low-density samples	High-density samples
BBM				
Elastic part	$\dot{\varepsilon}_v^e = -\frac{\kappa}{1+e_M}\frac{dp}{p} - \frac{\kappa_s}{1+e_M}\frac{ds_M}{s_M + p_{atm}}$	κ κ_s	0·010 0·022	0·010 0·041
Yield locus	$p_0 = p_c\left(\frac{p_0^*}{p_c}\right)^{(\lambda_{(0)}-\kappa)/(\lambda_{(s)}-\kappa)}$	p_o^*: MPa p_c: MPa r	0·14 0·005 0·65	0·38 0·005 0·72
	$\lambda(s) = \lambda(0)[r + (1-r)e^{-\beta_s}]$	$\lambda(0)$ β: MPa^{-1}	0·23 0·025	0·20 0·035
BExM				
Microstructural behaviour	$K_m = \frac{1+e_m}{\kappa_m}\hat{p}$	κ_m	0·045	
Interaction function (microstructural swelling)	$f_s = f_{s0} + f_{si}\left(1 - \frac{p}{p_0}\right)^{n_s}$	f_{s0} f_{si} n_s	−2·0 1 2	

Table 4. Initial conditions of the swelling pressure tests

Test label	Sample height: mm	Dry density of sample: g/cm^3	Total porosity, n_T	Macro-porosity, n_M	Micro-porosity, n_m	Macrop. suction, s_M: MPa	Microp. suction, s_m: MPa
MGR7	50	1·45	0·46	0·33	0·13	212	285
MGR9	100	1·45	0·46	0·33	0·13	284	321
RS2J	50	1·45	0·46	0·33	0·13	298	343
RS2B	50	1·60	0·40	0·16	0·24	207	237
RS2E	100	1·60	0·40	0·16	0·24	284	314
RS2F	120	1·60	0·40	0·16	0·24	284	314

between the two porosities. Eventually, however, they come together and remain in equilibrium for the remainder of the test. Interestingly, at the other two points the two porosities come into equilibrium before they are reached by the hydration front, that is before they exhibit any suction reduction. They also maintain this equilibrium condition throughout the rest of the test. The analysis suggests, therefore, that non-equilibrium between the two porosity levels is only likely to affect the early stages of the test. Fig. 13(b) shows the same information for one of the shorter (5 cm) samples: MGR7. The results obtained are qualitatively very similar, although hydration occurs earlier as the flow path is now shorter. The time required to reach steady-state condition is, as expected, also shorter.

The cause underlying the characteristic temporary drop in swelling pressure is the collapse of the macrostructure that, in the constitutive model, corresponds to reaching the LC yield surface in the BBM. This is illustrated in Fig. 14, where the stress paths (in macrostructural suction – vertical net stress space) followed by the same three points of test MGR9 are plotted. The initial position of the LC yield surface is also shown. In the section of the stress path that moves towards the LC surface, stress increase appears to be more significant than suction reduction. Once the LC yield surface is reached, the vertical stress drops to compensate the tendency of the macrostructure to collapse so that the sample length is kept constant. It can also be noted that the point of start of the collapse does not coincide exactly with the plotted LC; this is because, by then, the yield surface has moved slightly due to the interaction with the microstructural strains (MS, microstructure swelling) that develop from the very start of the test.

The interplay between the various aspects of the problem may be more readily seen by referring to Fig. 15, which contains details of the evolution of test MGR9 for the same three points considered above. Fig. 15(a) shows the evolution of vertical swelling pressures that are, naturally, the same for all three points because of equilibrium requirements. Fig. 15(b) shows the variations in time of the macrostructural and microstructural specific volume. There is a monotonic increase of microstructural porosity (or specific volume), the start of which is staggered in time as the various points respond to the different arrivals of the hydration front. The changes in macrostructural porosity are more complex. At the bottom of the specimen, the macrostructural porosity increases slightly at the beginning of the test because of suction reduction. However, on reaching the LC yield surface (indicated in the figure), there is a sharp reduction of macrostructural porosity due to structural collapse. This results in a translation of the LC yield surface towards the right, indicated by the increase in value of the saturated preconsolidation pressure, p_o^* (Fig. 15(c)). At the other two points, there is initially a reduction of the macrostructural porosity due to the compression applied by the swelling of

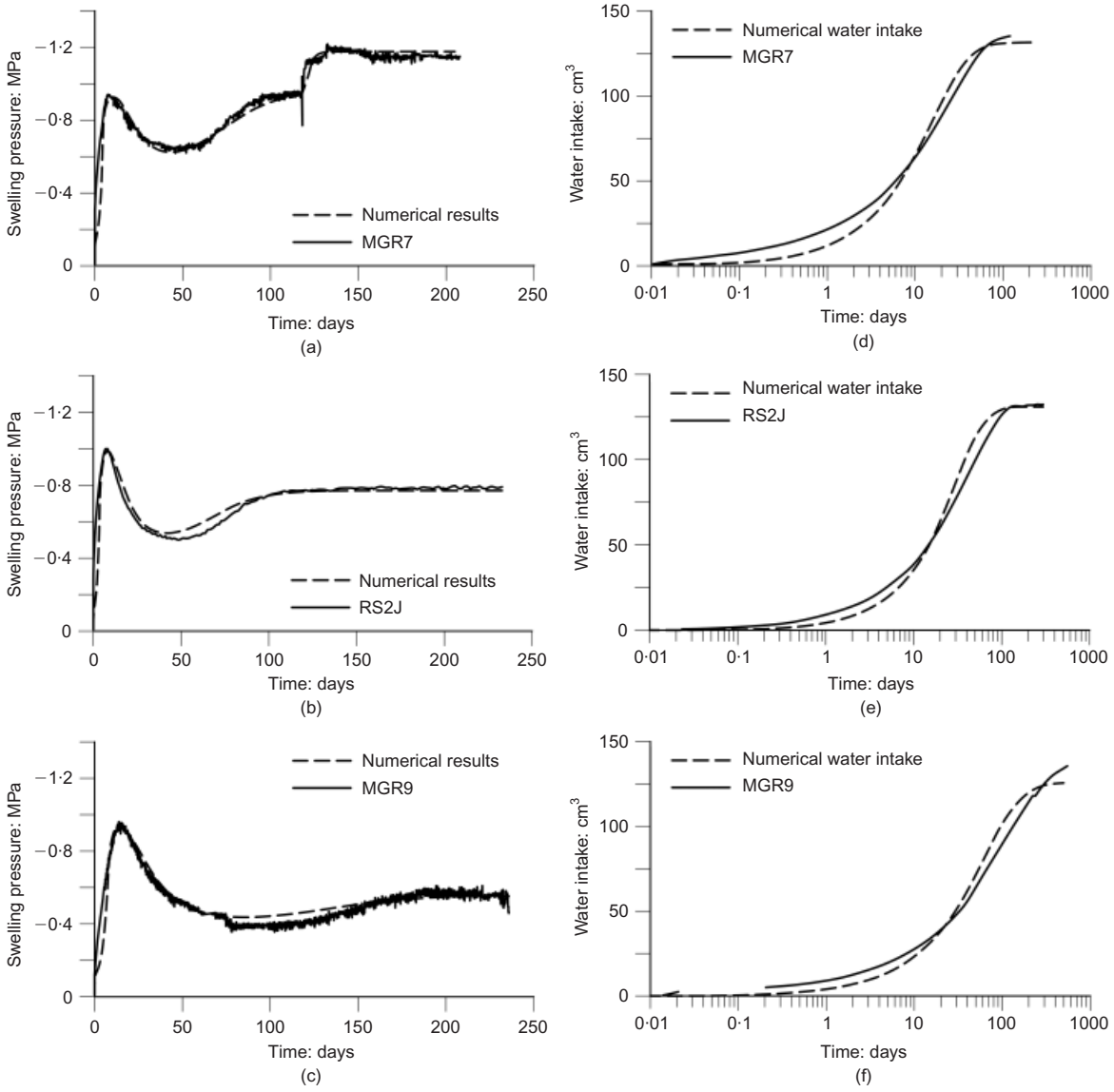

Fig. 12. Observations compared with computed results for tests on samples of 1·45 g/cm^3 dry density: (a)–(c) swelling pressure evolution for tests MGR7, RS2J and MGR9; (d)–(f) evolution of accumulated water intake for tests MGR7, RS2J and MGR9

the bottom part of the sample. Eventually, however, the points also reach the LC yield surface and collapse ensues. The final stage of reduction of macrostructural porosity is also partially associated with the increase of vertical stress caused by the swelling of the microstructure. In this final stage, the evolution of porosities is the same in all three points, consistent with the homogeneity of the samples observed at the end of the tests.

Microstructural observations

Determination of the pore size distribution could provide a valuable independent confirmation of the capability of the formulation to represent fabric changes of the material during hydration. Unfortunately, the pore size distribution of the samples after hydration was determined, using the MIP technique, only in the case of specimen MGR9. Four samples from different locations of the specimens were freeze-dried prior to pore size determination. The relationships between the cumulative intrusion porosity and entrance pore size for the four samples are shown in Fig. 16(a). It can be observed that there is a large amount of non-intruded porosity. Using these data, it is possible to derive the pore size density functions depicted in Fig. 16(b). By analogy with other materials (Wan *et al.*, 1995; Monroy, 2005; Romero *et al.*, 2005), it is likely that the large family of pores in the range of 200–500 nm was not present in the initial material but it is a consequence of the hydration process. Those pores would be the product of a reduction in size of larger macropores to accommodate the increase of micropore volume due to hydration. A direct check is not possible, however, as there were no MIP tests performed on the mixture before the test.

The proportions of porosity belonging to different ranges of pore sizes are listed in Table 5. The non-intruded volume has been ascribed to the ultra-microporosity smaller than 6 nm. Maintaining the boundary between microporosity and macroporosity at 100 nm, the final microstructural porosity falls in the range of 49–62%. Alternatively, Delage & Lefebvre (1984) suggested that microporosity could be estimated from the trapped volumes after mercury extrusion. In the present case, this criterion yields microporosity percentages ranging from 45% to 61%, quite consistent with the pore size density determination.

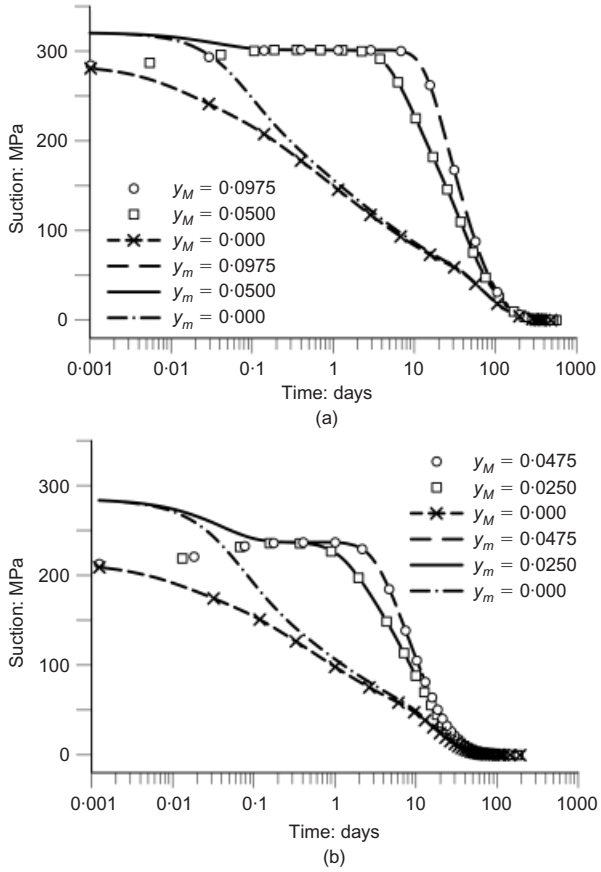

Fig. 13. Computed evolution of macrostructural and microstructural suctions at three different points of the sample: (a) test MGR9; (b) test MGR7

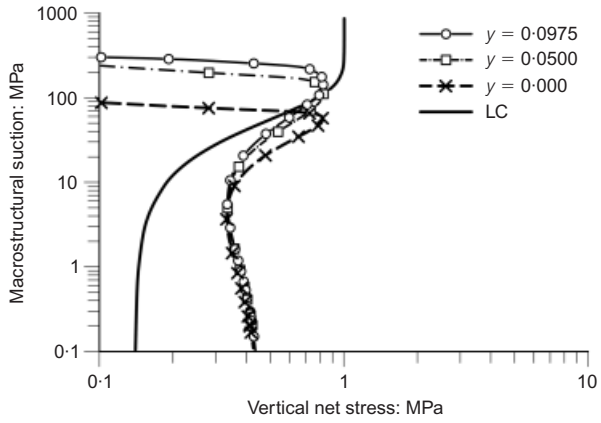

Fig. 14. Computed stress path (macrostructural suction–vertical stress) for three different points of sample MGR9. Only the initial LC yield surface is shown for clarity

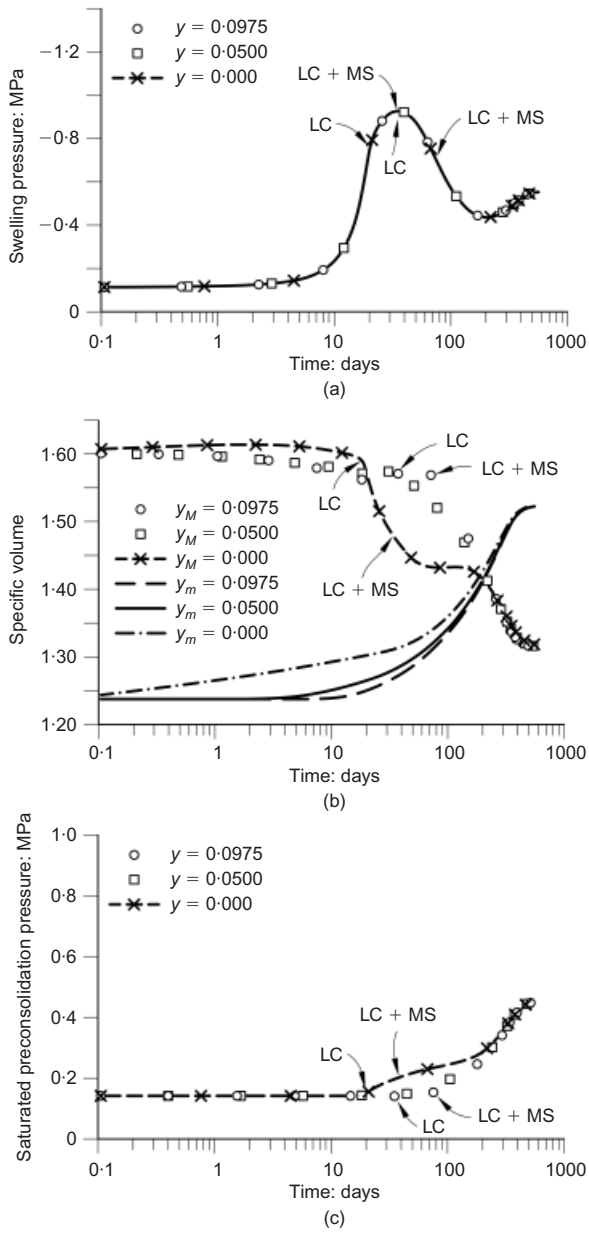

Fig. 15. Computed evolution of: (a) swelling pressure; (b) macrostructural and microstructural specific volumes; (c) saturated preconsolidation pressure for three points of test MGR9. Arrows indicate the point at which the various yield mechanisms are activated

In turn, the analyses predict that, in this test, microporosity increases from the initial value of 0·127 to 0·283 at the end of the test, whereas macroporosity decreases from 0·329 to 0·173. Therefore, the final microporosity represents 62% of the total pore volume, a rather satisfactory agreement with observations. The fact that the proportion of microporosity varies monotonically from the bottom to the top of the sample might suggest that, in spite of the long test duration and the constant values of macroscopic observations, the material was not completely saturated at the end of the test in the regions further away from the hydration boundary. This would imply the existence of a porosity level with a much lower leakage coefficient. This possibility, however, does not seem to prevent the model from achieving a good description of the macroscopic test results.

Swelling tests at dry density 1·60 g/cm^3

Three tests performed on samples with a dry density of 1·60 g/cm^3 (RS2B, RS2E and RS2F) are considered. Their lengths are 5, 10 and 12 cm respectively. The estimated initial porosities and suctions are listed in Table 4. Computed evolutions of swelling pressures compared with the measured values are shown in Figs 17(a)–17(c). Testing times ranged from 150 to 500 days depending on specimen length. The overall behaviour of these tests is similar to that of the looser samples but, in this case, the final swelling pressures are much higher and the swelling pressure drop after the first peak is comparatively smaller. At any rate, the model reproduces very satisfactorily the observed behaviour. The evolution of water intake is also well matched (Figs

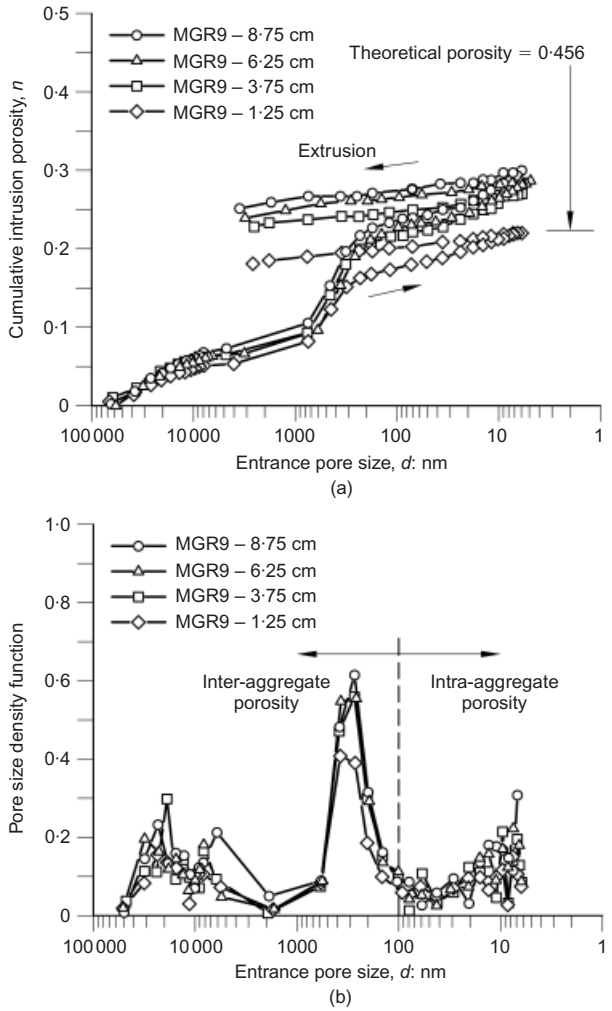

Fig. 16. Porosimetry results for four samples taken at the end of test MGR9: (a) cumulative intrusion porosities; (b) pore size density functions

17(d)–17(f)); some discrepancies at the end of the test have been attributed to small leakages in some of the very long-term tests.

Some results of the 10 cm sample (RS2E) are now presented so that they can be directly compared with the results of test MGR9. The evolutions of macrostructural and microstructural suctions at three different points (bottom, middle and top of the specimen) of test RS2F obtained in the analysis are plotted in Fig. 18. They are similar to those of the looser samples (Fig. 13). In this case, establishing equilibrium between the suctions at the two porosities takes a little longer and the onset of collapse is also delayed somewhat. The stress paths for the same three points are presented in Fig. 19. The initial LC is now further to the right to account for a denser macrostructure. It is also apparent that the drop in vertical stress after reaching the LC is now smaller if compared with the looser specimens (Fig. 14). Finally, Fig. 20 shows the computed evolution of swelling pressure, macrostructural and microstructural specific volumes, and saturated preconsolidation pressure for the same three points. Again the same overall behaviour as in test MGR9 is observed but now the relative variation of the macro and micro specific volumes is more limited than in the case of the tests on looser specimens. Also, in the final stages of the test, the evolution of porosities is the same in all three points, corresponding to a homogenised condition of the sample. The pattern of saturated preconsolidation pressure variation in time is again similar to that of the looser specimens, but a much higher final value is reached by the denser samples.

A LARGE-SCALE SEALING TEST

Description of the test

A large-scale sealing test (named the shaft sealing test) has been performed in the Hades underground research facility (URF) shown in Fig. 21. The URF is located in Mol (Belgium) and it has been excavated at a depth of 220 m in Boom Clay, an overconsolidated plastic clay of Rupelian age (28–34 million years). The sealing test has been performed in an experimental shaft located at the end of the main test drift (Fig. 22(a)). To this end, the bottom part of the shaft was filled with grout and the concrete lining was removed at the location of the seal. The sealed section is about 2·2 m in diameter and 2·25 m high. The sealing material is a mixture of 50% powder and 50% highly compacted pellets of FoCa clay, the same mixture as in the laboratory swelling pressure tests. The seal is kept in place with a top concrete lid about 1 m thick (Fig. 22(b)). A large number of sensors measuring pore water pressure, total stress, displacement and relative humidity were installed to follow the hydromechanical evolution of the seal and the surrounding host rock. In the seal, most instruments are located on six rods of stainless steel connected to a central tube. Those rods are located in two groups of three rods, each at two levels: the instrumented level top (ILT) and the instrumented level bottom (ILB). The ILT is located at 180 cm and the ILB at 65 cm from the bottom of the plug. Some instrumentation is also located at the hydration level top (HLT) and at the hydration level bottom (HLB). The instrumented sections are indicated in Fig. 22(b). Several filters inside the sealed section enabled artificial hydration to reduce the time required to attain saturation.

After coating the concrete plug with a resin, the clay mixture was installed using approximately 12 tons of powder/pellets mixture. The first 60 cm were compacted with a vibro-compactor specially designed for the project. After compaction the mixture had a dry density of 1·54 g/cm^3. The rest of the mixture of powder and pellets was not compacted in order to avoid damage of the sensors, resulting in a dry density of 1·39 g/cm^3. A top view of the shaft during backfill installation has been provided in Fig. 1. Some details of the installation are shown in Fig. 23.

Table 5. Pore size distribution measured in four samples obtained from test MGR9 after hydration

	Entrance pore size	Percentage of total porosity			
		y = 8·75 cm	y = 6·50 cm	y = 3·25 cm	y = 1·25 cm
Macroporosity	>1000 nm	~21	~20	~19	~17
Mesoporosity	100–1000 nm	~30	~30	~28	~21
Microporosity	20–100 nm	~ 5	~5	~ 6	~5
Ultra-microporosity	<20 nm	~44	~45	~47	~57

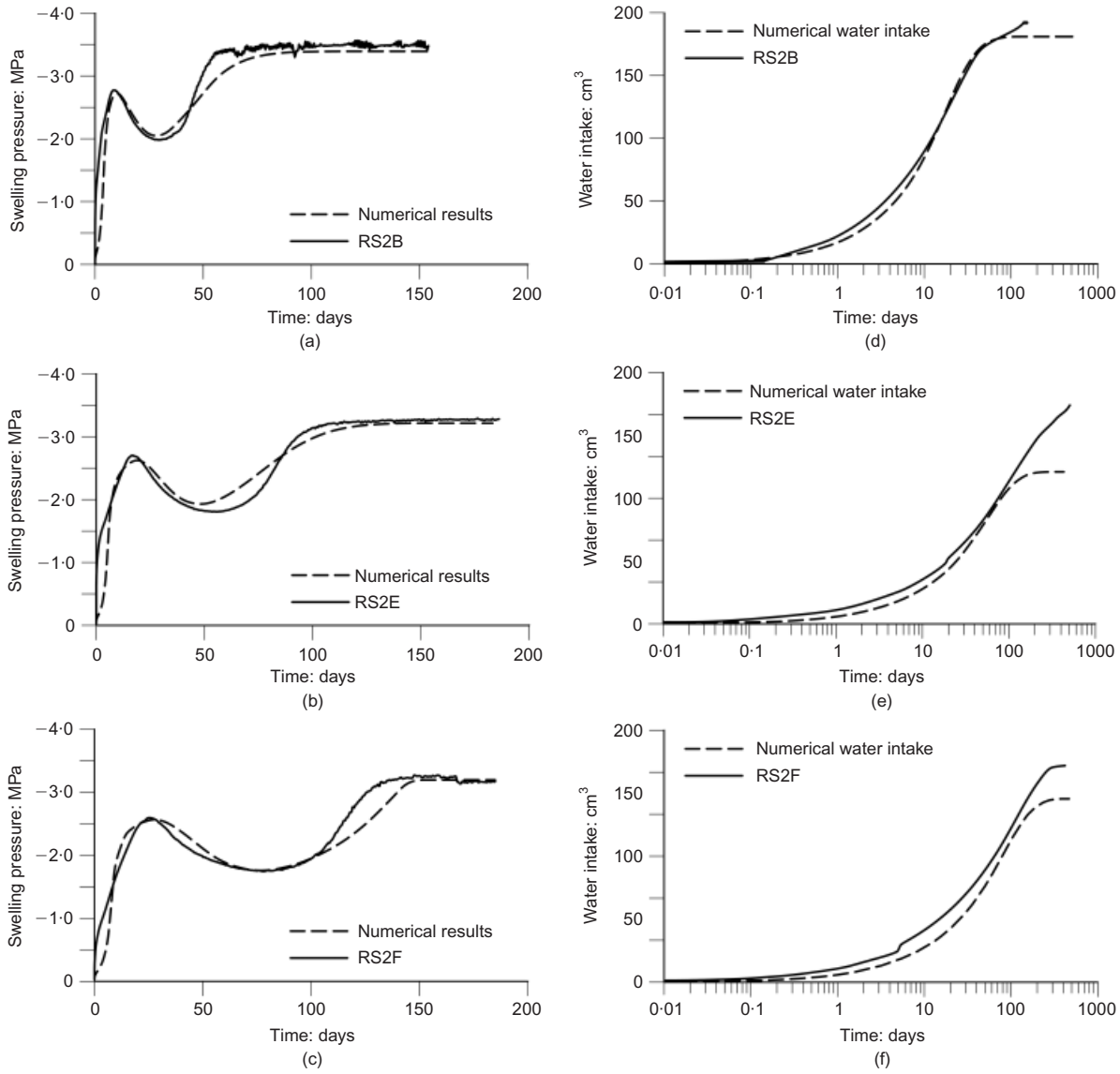

Fig. 17. Observations compared with computed results for tests on samples of 1·60 g/cm^3 dry density: (a)–(c) swelling pressure evolution for tests RS2B, RS2E and RS2F; (d)–(f) evolution of accumulated water intake for tests RS2B, RS2E and RS2F

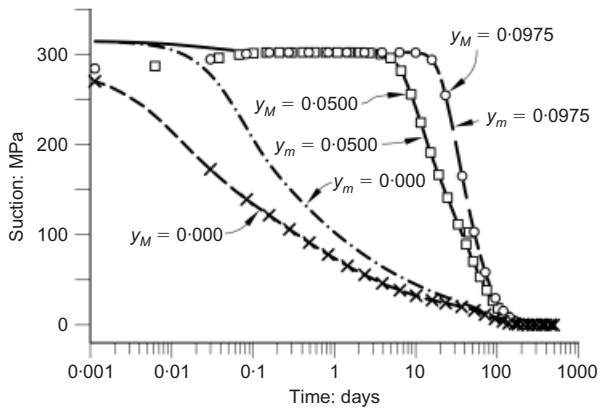

Fig. 18. Computed evolution of macrostructural and microstructural suctions at three different points of test RS2F

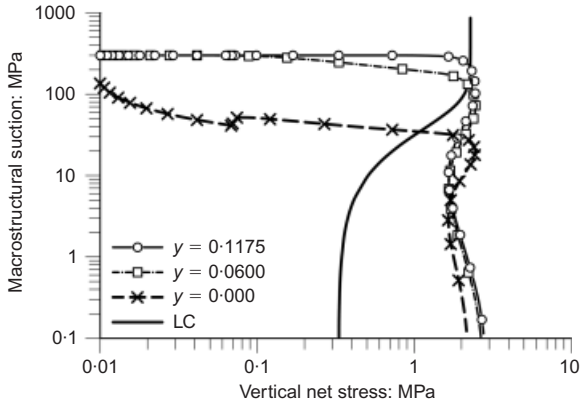

Fig. 19. Computed stress path (macrostructural suction–vertical stress) for three different points of sample RS2E. Only the initial LC yield surface is shown for clarity

After backfilling the shaft and closing the seal, a 7-month period was allowed to elapse to achieve steady-state conditions in the zone around the test. Afterwards, artificial hydration was applied during 6 years. Some leakage problems occurred in the early stages of the test and hydration had to be stopped and re-started on some occasions. The water injection pressure was increased gradually up to a value of 300 kPa, approximately, measured at the elevation

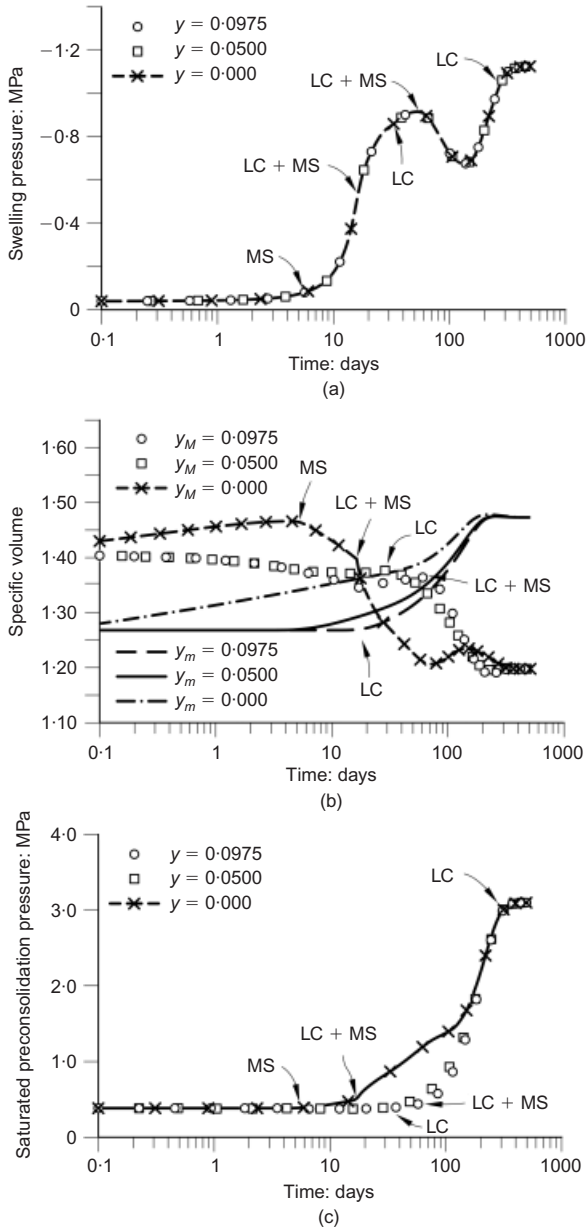

Fig. 20. Computed evolution of: (a) swelling pressure; (b) macrostructural and microstructural specific volumes; (c) saturated preconsolidation pressure for three points of test RS2E. Arrows indicate the point at which the various yield mechanisms are activated

of the main drift. After seal saturation, various gas and liquid permeability tests have been performed but only the hydration stage is considered in this paper.

Seal hydration and modelling

The hydration of the seal has been simulated using the theoretical formulation outlined above. The finite-element mesh used in the coupled hydromechanical analysis is depicted in Fig. 24 together with the main boundary conditions. Advantage has been taken of the basically axisymmetric nature of the test. The initial characteristics of the pellets–powder mixture installed in the shaft are listed in Table 6. The hydraulic and mechanical parameters of the backfill material are the same as those used in the analyses of the swelling pressure tests (Tables 2 and 3). The challenge is to be able to cover a large-scale span (from laboratory to field conditions) using the same formulation, conceptual model and parameters. The estimated partition of porosities and the initial suction values are given in Table 7. As the natural Boom Clay parameters have only a limited impact on results, they are not given here. Boom Clay parameters and the procedures used for their determination are reported in Gens *et al.* (2009a). Some selected results concerning suctions and stresses in the sealing material are now presented.

Figure 25(a) shows the variation in time of the suction measured in the relative humidity sensors located on the rods of the ILT, an instrumentation level located in the uncompacted part of the backfill. There are only two sensors because the one oriented towards the west failed from the start. The sensor closer to the rock (RH-S-ILT-E) appeared to hydrate only a little faster than the one placed near the centre (RH-S-ILT-N), suggesting that the natural hydration from the host Boom Clay is not dominant. The computed suction evolutions are quite close to observations in this case and the analysis also shows a somewhat faster hydration in the sensor closer to the rock boundary. The readings of the relative humidity sensors located at the ILB are plotted in Fig. 25(b). In this case, the instrumented level is situated in the compacted backfill but very close to the boundary between the two zones. Now, there are large differences between the readings of the different sensors, significantly larger than those obtained in the modelling. The analysis also suggests that hydration should be slower at this level because of the lower permeability of the compacted material. This is borne out by the observations except for the sensor placed quite close to the central injection tube (RH-S-ILB-W). It is strongly suspected that a direct connection between hydration tube and the zone of the sensor was established during one of the injection pressure increase episodes.

The evolutions of vertical stresses at 16 points located at different heights of the seal are shown in Fig. 26 and compared with the results of the analysis. From top to bottom they are located in (a) hydration level top, (b) instrumentation level top, (c) instrumentation level bottom and (d) hydration level bottom. The usual difficulties associated with trying to measure stresses precisely are apparent in the plots. It can also be noted that stress development is not axisymmetric; departures from that condition vary depending on the instrumentation level considered. The response of the sensors does not appear to be simultaneous with hydration; this may be perhaps attributed in part to a lack of close contact with the backfill after installation. In spite of those difficulties, the analysis appears to give correctly the rough magnitude of the hydration swelling pressure as well as the rate of stress increase in the later stages of the test. Naturally, the axisymmetric analysis does not discriminate between different directions. It should be stressed that the same set of parameters used in the modelling of the laboratory tests has been adopted for the analysis of the shaft sealing test.

It is interesting to observe that the model only predicts a rather muted drop in the value of the vertical stress in the second year of the test. Although the density of the backfill is low, the effect of macrostructural collapse is minor because it is averaged out among different zones. This is a consequence of the very different scale of this test as compared with the laboratory ones. At small scales, different stages of macrostructural collapse may be occurring at the same time in practically the entire sample, leading to a large drop in swelling stress. At the scale of a field case, this simultaneity is more unlikely and the collapse in some zones is at least partially compensated by the non-collapsing behaviour of other zones. It should be noted that the test observations do not record any instance of sharp vertical

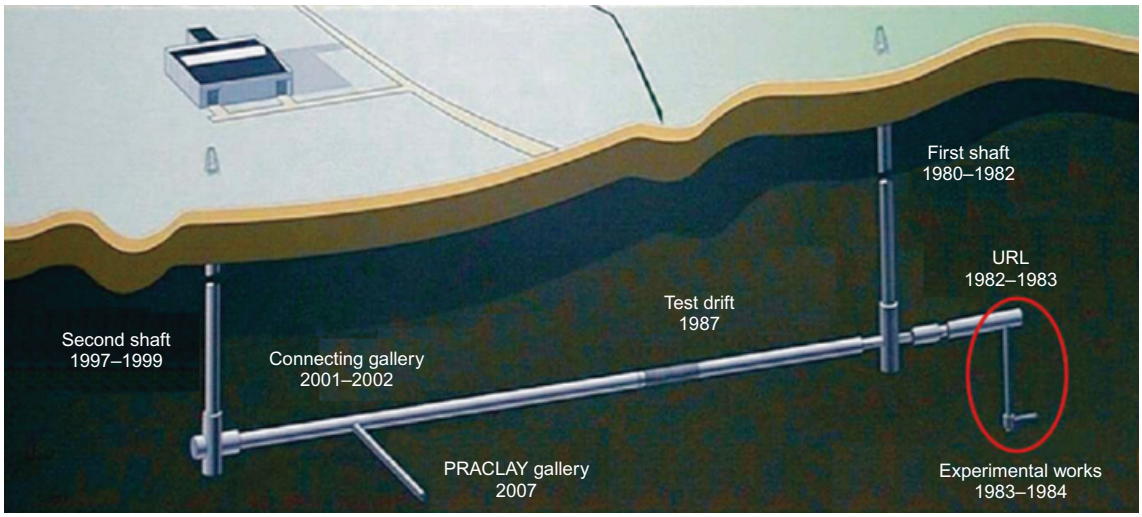

Fig. 21. The Hades underground research facility: the experimental shaft where the sealing test was installed is indicated

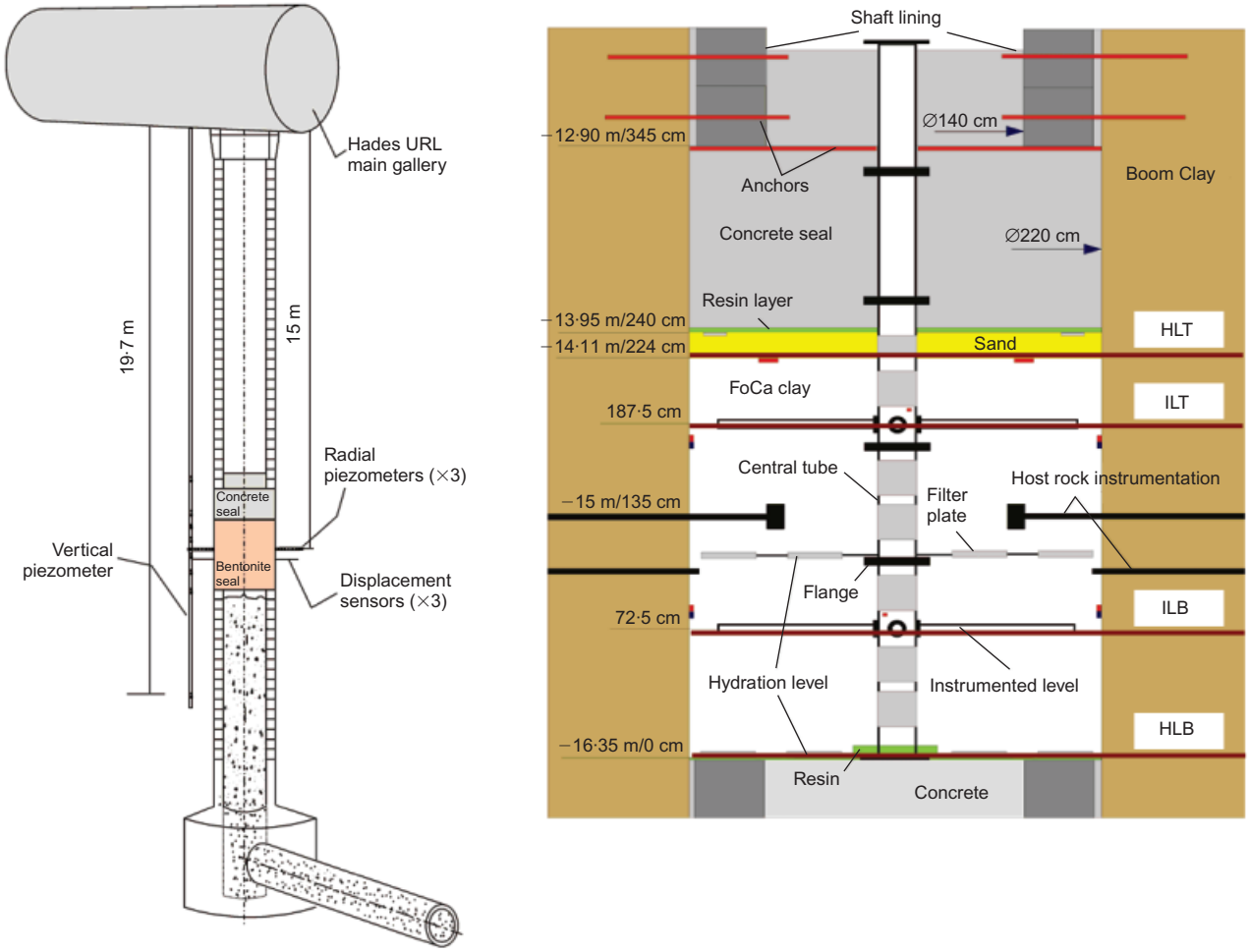

Fig. 22. (a) Schematic overview of the location of the seal inside the experimental shaft. (b) Layout of the test including instrumentation levels. HLT: hydration level top; ILT: instrumentation level top; ILB: instrumentation level bottom; HLB: hydration level bottom

stress reduction, although some slowing down in the rate of increase (or even some local stress reductions) can be noted in some sensors during the second year of testing. In addition, analysis results and observations largely agree in the steady increase of vertical stress at the end of the test.

CONCLUDING REMARKS

The use of compacted mixtures of bentonite powder and bentonite pellets as backfill material in underground repositories for nuclear waste is an attractive proposition because it reduces significantly the compaction effort that is required

(a) (b)

Fig. 23. (a) Rod instrumented with total stress, water pressure, displacement and suction sensors. (b) Installation of a piezometer in the host medium

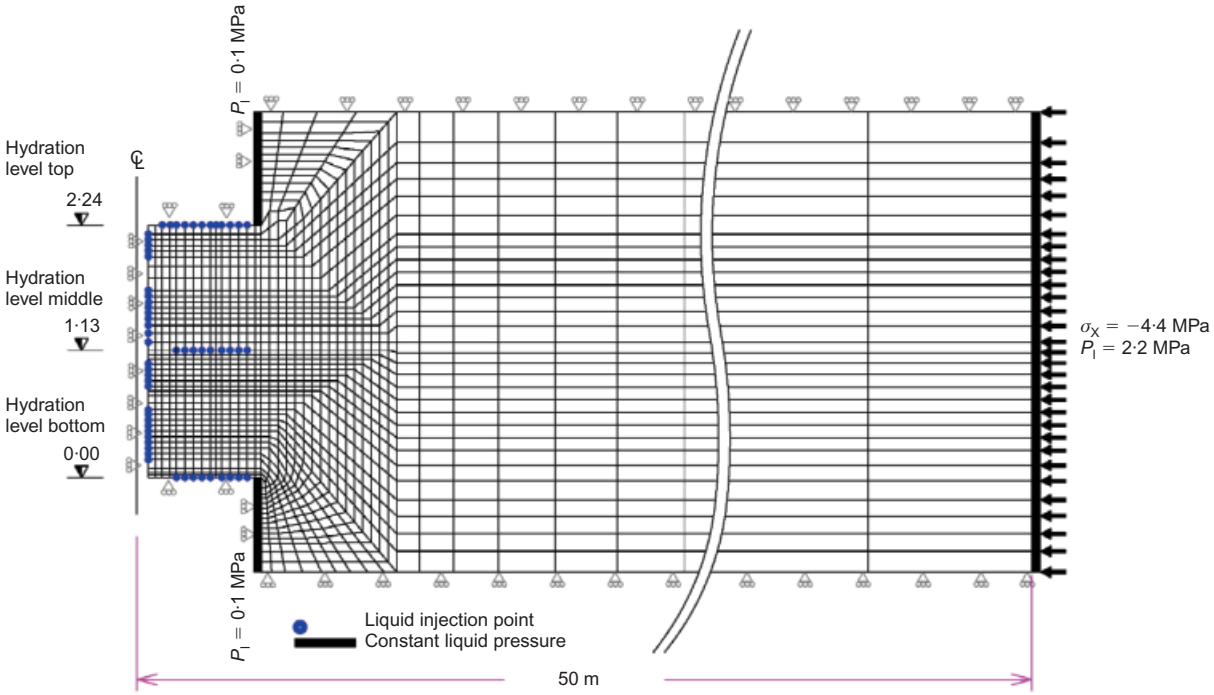

Fig. 24. Axisymmetric finite-element mesh and boundary conditions used in the analysis of the shaft sealing test

Table 6. Main characteristic of the pellets/powder mixture installed in the experimental shaft

Height: cm	Void ratio of mixture	Dry density of mixture: g/cm^3	Initial water content of mixture: %	Dry density of pellets: g/cm^3	Initial water content of pellets: %	Dry density of powder: g/cm^3	Initial water content of powder: %
Compacted zone							
60	0·734	1·543	6·00	1·894	4·49	1·302	7·51
Uncompacted zone							
164	0·929	1·387	6·00	1·894	4·49	1·093	7·51

to achieve the value of dry density needed to provide an adequate swelling potential on hydration. However, the heterogeneous fabric of the material results in a quite complex behaviour during hydration.

In the paper, it has been demonstrated that a double porosity approach, involving both hydraulic and mechanical aspects, is able to provide the necessary theoretical framework to undertake satisfactorily the hydromechanical model-

Table 7. Initial conditions of the pellets–powder mixture used in the shaft sealing test

	Dry density of mixture: g/cm^3	Total porosity, n_T	Macrostructural porosity, n_M	Microstructural porosity, n_m	Macrostructural suction, s_M: MPa	Microstructural suction, s_m: MPa
Compacted seal	1·543	0·423	0·278	0·145	272	279
Uncompacted seal	1·387	0·482	0·366	0·116	280	308

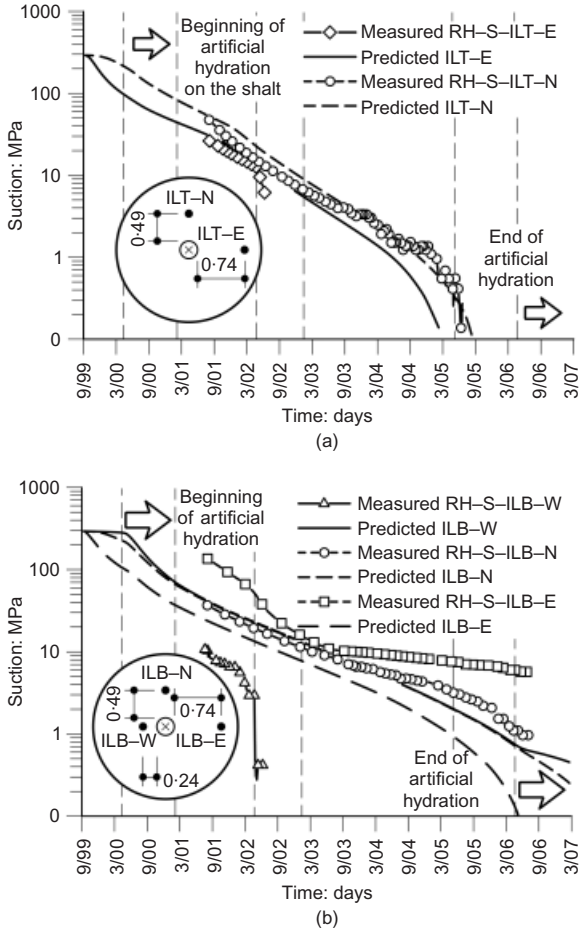

Fig. 25. Variation of suction with time: computed results and observations: (a) instrumented level top; (b) instrumented level bottom

ling of this material. The formulation (and associated computer code) results in close quantitative reproduction of a number of swelling pressure tests performed on samples of different densities and lengths. In addition, a detailed examination of the computational results provides valuable insights and understanding of the basic processes that underlie the observed macroscopic behaviour. Moreover, microfabric information using X-ray tomography and MIP provide additional support for the conceptual approach adopted.

Using the same parameters as in the modelling of laboratory tests, the application of the formulation to a field-scale long-term sealing test performed in the Hades URF has resulted in a quite adequate description of the main behaviour features of the backfill during hydration. The capability of the formulation to span over quite large ranges of space and time scales is thus established. In addition, because the formulation is based, albeit roughly, on the actual composition of the material, it is capable of providing important insights that are key in the building up of confidence in the eventual repository design. In fact, the conceptual approach developed in the context of the research reported in this paper is quite general and it can be readily applied to other types of heterogeneous compacted soils. A better understanding of their hydromechanical behaviour should thereby ensue.

ACKNOWLEDGEMENTS

The work reported has been co-funded by ANDRA, CIEMAT, ONDRAF-NIRAS and the European Commission (EC contract FIKW-CT-2000-00010). The support of the Spanish Ministry of Science and Innovation through grant BIA 2008-06537 is also gratefully acknowledged.

APPENDIX

A detailed description of the BBM model can be found in Alonso *et al.* (1990). Here, the more relevant equations of the particular version of the BBM used are presented. The model is defined in terms of the following stress invariants

$$p = \frac{1}{3}(\sigma_x + \sigma_y + \sigma_z) \tag{16}$$

$$J^2 = 0{\cdot}5 \text{ trace } (\boldsymbol{s}^2) \tag{17}$$

$$\theta = -\frac{1}{3}\sin^{-1}\left(1{\cdot}5\sqrt{3}\ \det\ \boldsymbol{s}/J^3\right) \tag{18}$$

$$\boldsymbol{s} = \boldsymbol{\sigma} - p\boldsymbol{I} \tag{19}$$

$$\boldsymbol{\sigma} = \boldsymbol{\sigma}_t - \boldsymbol{I}p_f \tag{20}$$

where $p_f = p_g$ if $p_g > p_l$, otherwise $p_f = p_l$. p_g is the gas pressure and p_l is the liquid pressure. $\boldsymbol{I}$ is the identity tensor.

The LC yield surface (F_{LC}) can be expressed as

$$F_{LC} = 3J^2 - \left[\frac{g(\theta)}{g(-30)}\right]^2 M^2(p + p_s)(p_o - p) = 0 \tag{21}$$

where M is the slope of the critical state, p_o is the apparent unsaturated isotropic preconsolidation pressure, g is a function of Lode's angle and p_s considers the dependence of shear strength on suction. The following relationships complete the definition of the yield surface

$$p_s = ks_M \tag{22}$$

$$p_0 = p_c\left(\frac{p_0^*}{p_c}\right)^{\left(\lambda_{(0)}-\kappa\right)/\left(\lambda_{(s)}-\kappa\right)} \tag{23}$$

where k is a parameter that accounts for the increase of shear strength with suction, p_c is a reference stress, κ is the elastic stiffness parameter for changes in net mean stress, p_0^* is the preconsolidation net mean stress for saturated conditions. $\lambda_{(s)}$ is the compressibility parameter for changes in net mean stress for virgin states of the soil that depends on macrostructural suction, s_M, according to

$$\lambda_{(s)} = \lambda_{(0)}\left[r + (1-r)e^{-\beta s_M}\right] \tag{24}$$

where r is a parameter which defines the minimum soil compressibility (at infinity suction) and β is a parameter which controls the rate of decrease of soil compressibility with macrostructural suction.

The hardening law is expressed as a rate relation between

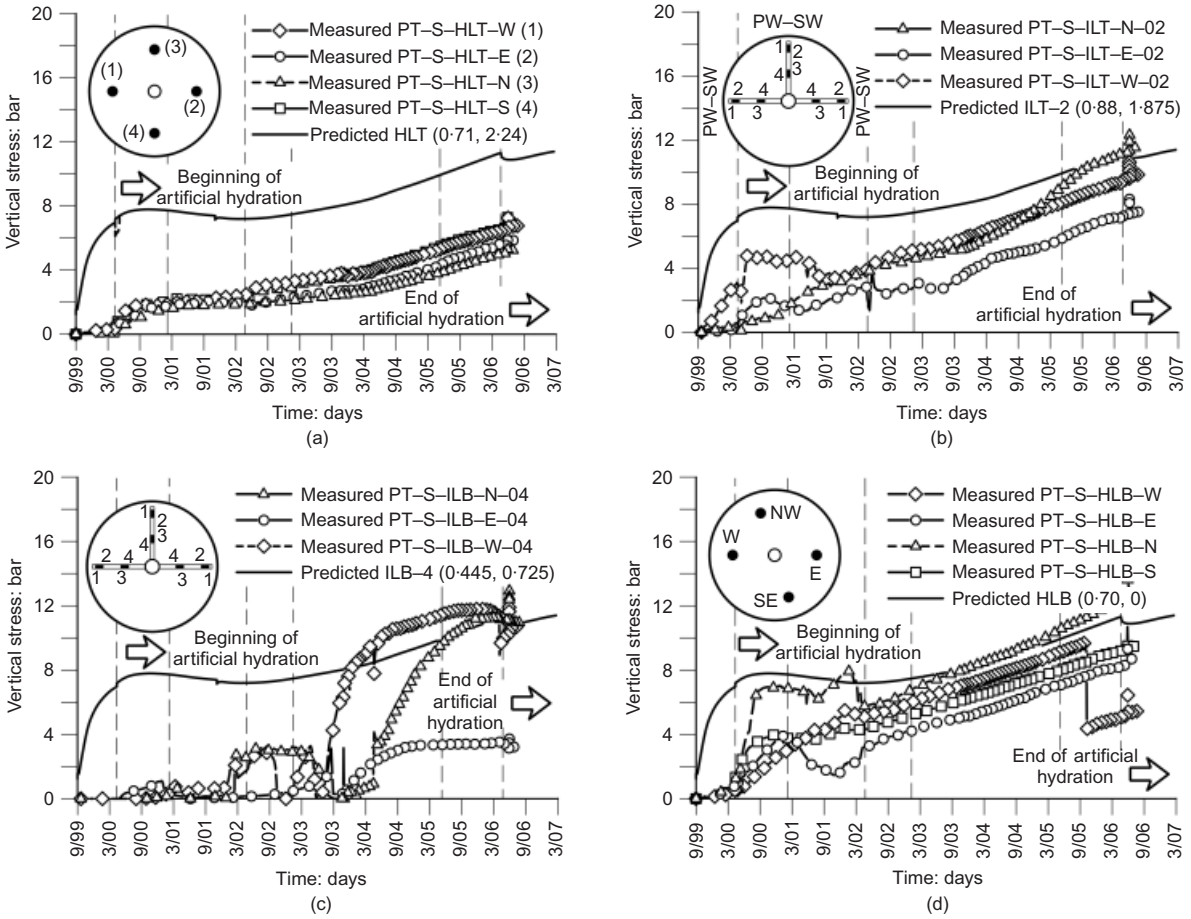

Fig. 26. Variation of vertical stresses with time: computed results and observations: (a) hydration level top, $r = 0{\cdot}71$ m; (b) instrumented level top, $r = 0{\cdot}88$ m; (c) instrumented level bottom, $r = 0{\cdot}445$ m; (d) hydration level bottom, $r = 0{\cdot}70$ m (r is the radial coordinate)

volumetric plastic strain and the saturated isotropic preconsolidation stress, p_0^*, as

$$\frac{\dot{p}_0^*}{p_0^*} = \frac{(1+e_M)}{(\lambda_{(0)}-\kappa)}\dot{\varepsilon}_{vM}^p \tag{25}$$

where e_M is the macrostructural void ratio, κ is the elastic compression index for changes in net mean stress and $\lambda_{(0)}$ is the compression index for changes in net mean stress for virgin states of the soil in saturated conditions.

Regarding the direction of the plastic strain increment, a non-associated flow rule in the plane $s_M = \text{constant}$

$$G = \alpha 3J^2 - \left[\frac{g(\theta)}{g(-30)}\right]^2 M^2(p+p_s)(p_0-p) = 0 \tag{26}$$

where α is determined from the condition that the flow rule predicts zero lateral strains in a K_0 stress path.

Finally, the macrostructural elastic volumetric strains are computed as

$$\dot{\varepsilon}_{vM}^e = -\frac{\kappa}{1+e_M}\frac{\mathrm{d}p}{p} - \frac{\kappa_s}{1+e_M}\frac{\mathrm{d}s_M}{s_M+p_{atm}} \tag{27}$$

where κ and κ_s are model parameters and p_{atm} is the atmospheric pressure (100 kPa).

REFERENCES

Aifantis, E. (1980). On the problem of diffusion in solids. *Actha Mechanica* **37**, No. 3–4, 65–296.

Alonso, E. E., Gens, A & Josa, A. (1990). A constitutive model for partially saturated soils, *Géotechnique* **40**, No. 3, 405–430, **doi**: 1680/geot.1990.40.3.405.

Barrenblatt, G., Zeltov, I. & Kochina, N. (1960). Basic concepts in the theory of seepage of homogeneous liquids in fissured rocks. *Pirkl. Mater. Mekh*. **24**, 852–864.

Callari, C. & Federico, F. (2000). FEM validation of a double-porosity elastic model for consolidation of structurally complex clayey soils. *Int. J. Numer. Analyt. Methods Geomech*. **24**, No. 4, 367–402.

Castellanos, E., Villar, M. V., Romero, E., Lloret, A. & Gens, A. (2008). Chemical impact on the hydro-mechanical behaviour of high density FEBEX bentonite. *Phys. Chem. Earth* **33**, Suppl. 1, S516–S526.

Cui, Y., Yahia-Aissa, M. & Delage, P. (2002). A model for the volume change behaviour of heavily compacted swelling clays. *Engng Geol*. **64**, No. 2–3, 233–250.

Delage, P. & Lefebvre, G. (1984). Study of the structure of a sensitive Champlain clay and its evolution. *Can. Geotech. J.* **21**, No. 1, 21–35.

Delage, P., Howat, M. D. & Cui, Y. (1998). The relationship between suction and swelling properties in a heavily compacted unsaturated clay. *Engng Geol*. **50**, No. 1–2, 31–48.

Gens, A. (2003). The role of geotechnical engineering for nuclear energy utilisation. *Proc. 13th Eur. Conf. Soil Mech. Geotech. Engng, Prague* **3**, 25–67.

Gens, A. (2010). Soil–environment interactions in geotechnical engineering. 47th Rankine Lecture. *Géotechnique* **60**, No. 1, 3–74, **doi**: 10.1680/geot.9.P.109.

Gens, A. & Alonso, E. E. (1992). A framework for the behaviour of unsaturated expansive clays. *Can. Geotech. J.* **29**, No. 6, 1013–1032.

Gens, A., Alonso, E. E., Lloret, A. & Batlle, F. (1993). Prediction of long term swelling of expansive soft rock: a double-structure approach. In *Geotechnical engineering of hard soils–soft rocks* (eds A. Anagnostopoulos, F. Schlosser, N. Kalteziotis and R. Frank), Vol. 1, pp. 495–500. Rotterdam: Balkema.

Gens, A., García-Molina, A. J., Olivella, S., Alonso, E. E. &

Huertas, F. (1998). Analysis of a full scale in situ test simulating repository conditions. *Int. J. Numer. Analyt. Methods Geomech*. **22**, No. 7, 515–548.

Gens, A., Filippi, M., Vallejan, B. *et al.* (2009a). *RESEAL II project – Final report on modelling (WP4)*, SCK–CEN report ER-80. Brussels: SCK–CEN (Studiecentrum voor Kernenergie–Centre d'Etude de l'énergie Nucléaire (Belgian Nuclear Research Centre)).

Gens, A., Sánchez, M., Guimarães, L. do N. *et al.* (2009b). A full-scale in situ heating test for high-level nuclear waste disposal: observations, analysis and interpretation. *Géotechnique* **59**, No. 4, 377–399, **doi**: 10.1680/geot.2009.59.4.377.

Ghafouri, H. & Lewis, R. (1996). A finite element double porosity model for heterogeneous deformable porous media. *Int. J. Numer. Analyt. Methods Geomech* **20**, No. 11, 831–844.

Guimarães, L. do N., Gens, A. & Olivella, S. (2007). Coupled thermo-hydro-mechanical and chemical analysis of expansive clay subject to heating and hydration. *Transp. Porous Media* **66**, No. 3, 341–372.

IAEA (International Atomic Energy Agency) (1990). *Sealing of underground repositories for radioactive wastes*, IAEA Technical Report Series No. 319. Vienna: IAEA.

Imbert, V. & Villar, M. V. (2006). Hydro-mechanical response of a bentonite pellets/powder mixture upon infiltration. *Appl. Clay Sci*. **32**, No. 3–4, 197–209.

Imbert, C., Fleureau, J.-M., Kheirbek-Saoud, S. & Deprez, L. (1997). *Caracterisation hydrique des materiaux de l'experience PRACLAY.* Fontenay-aux-roses, France: Commissariat à l'energie atomique (CEA), Technical Report (in French).

Khalili, N., Valliappan, S. & Wan, C. (1999). Consolidation of fissured clay. *Géotechnique* **49**, No. 1, 75–89, **doi**: 10.1680/geot.1999.49.1.75.

Lloret, A., Villar, M. V., Sánchez, M. *et al.* (2003). Mechanical behaviour of heavily compacted bentonite under high suction changes. *Géotechnique* **53**, No. 1, 27–40, **doi**: 10.1680/geot.2003.53.1.27.

Marcial, D. (2003). *Comportement hydromécanique et microstructural des matériaux de barrière ouvragée*. PhD thesis, École Nationale des Ponts et Chaussées, France.

Michaux, L. & Loubignac, J. M. (1995). *Evolution de la microstructure de l'argile Fo-Ca-7 compactée lors d'un cycle d'hydration/deshydration à 25°C*. Fontenay-aux-roses, France: Commissariat à l'energie atomique, Technical Report (in French).

Monroy, R. (2005). *The influence of load and suction changes on the volumetric behaviour of compacted London Clay.* PhD thesis, Imperial College, London.

Olchitzky, E. (2002). *Couplage hydromécanique et perméabilité d'une argile gonflante non saturée sous sollicitations hydriques et thermiques: courte de sorption et perméabilité à l'eau*. PhD thesis, Ecole Nationale des Ponts et Chaussées, Marne La Vallée, Paris, France (in French).

Olivella, S., Gens, A., Carrera, J. & Alonso, E. E. (1996). Numerical formulation for a simulator (CODE_BRIGHT) for the coupled analysis of saline media. *Engng Comput*. **13**, No. 7, 87–112.

Pusch, R. (1994). *Waste disposal in rock*, Developments in Geotechnical Engineering, Vol. 76. Amsterdam: Elsevier.

Romero, E. (1999). *Characterization and thermo-hydro-mechanical behaviour of unsaturated Boom clay: an experimental study.* PhD thesis, Universitat Politecnica de Catalunya, Spain.

Romero, E., Hoffmann, C., Castellanos, E., Suriol, J. & Lloret, A. (2005). Microstructural changes of compacted bentonite induced by hydro-mechanical actions. In *Advances in understanding engineered clay barriers* (eds E. E. Alonso and A. Ledesma), pp. 193–202. Rotterdam: Balkema.

Sánchez, M. (2004). *Thermo-hydro-mechanical coupled analysis in low permeability media*. PhD thesis, Universitat Politecnica de Catalunya, Spain.

Sánchez, M., Gens, A., Guimarães, L. do N. & Olivella, S. (2005). A double structure generalized plasticity model for expansive materials. *Int. J. Numer. Analyt. Methods Geomech*. **29**, No. 8, 751–787.

Touret, O., Pons, C., Tessier, D. & Tardy, Y. (1990). Etude de la répartition de l'eau dans des argiles saturées Mg^{2+} aux fortes teneurs en eau. *Clay Minerals* **25**, No. 2, 217–223.

Van Geet, M., Volckaert, G. & Roels, S. (2005). The use of microfocus X-ray computed tomography in characterising the hydration of a clay pellet/powder mixture. *Appl. Clay Sci*. **29**, No. 2, 73–87.

Van Genuchten, M. T. (1980). A closed-form equation for predicting the hydraulic conductivity of unsaturated soils. *Soil Sci. Soc. Am. J.* **44**, 892–898.

Volckaert, G., Bernier, F., Alonso, E. *et al.* (1996). *Thermal-hydraulic-mechanical and geochemical behaviour of the clay barrier in radioactive waste repositories (model development and validation)*, Nuclear Science and Technology, EUR 16744. Luxembourg: Commission of the European Communities.

Volckaert, G., Dereeper, B., Put, M. *et al.* (2000). *A large-scale* in situ *demonstration test for repository sealing in an argillaceous host rock RESEAL project – phase I*, EUR 19612, 273 pp. Luxembourg: European Commission.

Wan, A. W. L., Gray, M. N. & Graham, J. (1995). On the relations of suction, moisture content and soil structure in compacted clays. *Proc. 1st Int. Conf. Unsaturated Soils, Paris* **1**, 215–222. Rotterdam: Balkema.

Warren, J. & Root, P. (1963). The behaviour of naturally fracturated reservoirs. *Soc. Petrol. Engrs J.* **228**, No. 8, 244–255.

Wilson, R. & Aifantis, E. (1982). On the theory of consolidation with double porosity. *Int. J. Engng Sci*. **20**, No. 9, 1019–1035.

Yahia-Aïssa, M., Delage, P. & Cui, Y. J. (2000). Volume change behaviour of a dense compacted swelling clay under stress and suction changes. In *Experimental evidence and theoretical approaches in unsaturated soils* (eds A. Tarantino and C. Mancuso), pp. 65–74. Rotterdam: Balkema.